J. Fluid Mech. (1997), *vol.* 345, *pp.* 133–164. Printed in the United Kingdom

© 1997 Cambridge University Press

Spatial numerical simulation of boundary layer transition: effects of a spherical particle

By E. M. SAIKI† AND S. BIRINGEN

Department of Aerospace Engineering Sciences, University of Colorado, Boulder, CO 80309, USA.

(Received 4 January 1996 and in revised form 6 April 1997)

In the present study, the effects of an isolated stationary spherical particle on the transition process in a flat-plate boundary layer are examined by a spatial direct numerical simulation. The full three-dimensional time-dependent incompressible Navier–Stokes equations are integrated by a time-splitting method and discretized spatially by a high-order finite difference/spectral method. A virtual boundary technique defining the no-slip boundary of a sphere is implemented within the Cartesian geometry of the computational grid.

Two numerical simulations which consider the effects of the sphere on the boundary layer are presented. The subcritical Reynolds number case reveals the appearance of hairpin vortices shed into the sphere wake which decay as they are convected downstream. The initial interaction of the sphere and the boundary layer produces a three-dimensional isolated disturbance comprising a wave part and a transient part. The decaying transient part is convected downstream at the local mean velocity, while the wave part induces a decaying Tollmien–Schlichting wave in the flow field.

In the second case, an increase in the Reynolds number results in a wedge of incipient turbulent flow downstream of the sphere. The development of the wake of the sphere is dominated by the appearance of an isolated disturbance which rapidly breaks down forming a structure resembling a turbulent spot. It is demonstrated that the transition induced by a sphere in the boundary layer is due to a mechanism related to bypass transition.

1. Introduction

The effects of particulates on boundary layer transition have received considerable attention as a bypass mechanism with regard to vehicles moving through a particulate environment. Individual particulates affect transition by entering the boundary layer causing additional fluid motion through shedding of vortices and/or impacting the surface creating an isolated, three-dimensional roughness element. Experimental studies by Blackwelder *et al.* (1992) examined the influence of a moving sphere with a diameter of roughly one-third of the boundary layer thickness, δ. Their flow visualization study revealed the production of a turbulent spot by an isolated particle entering the boundary layer.

The experiments of Hall (1967) investigated the flow field arising from both elevated and surface-mounted spheres in the boundary layer. In agreement with Mochizuki (1961) and other roughness element studies, Hall (1967) observed either laminar

† Present address: National Center for Atmospheric Research, PO Box 3000, Boulder, CO 80307-3000, USA.

https://doi.org/10.1017/S0022112097006198 Published online by Cambridge University Press

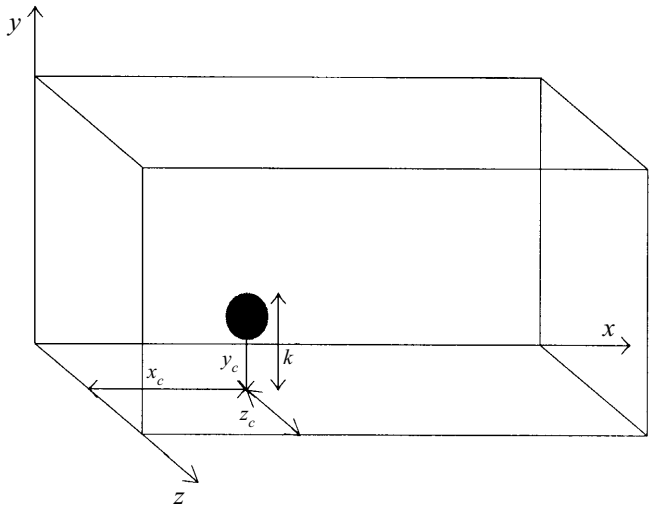


FIGURE 1. Schematic of the sphere in the boundary layer. The variables indicated are in non-dimensional form.

shedding of vortices which decayed as they were convected downstream or the development of a turbulent wedge dependent upon the particle Reynolds number, Re_d, and the height of the sphere with respect to the boundary layer thickness, i.e. k^*/δ_p. Here, δ_p is the boundary layer thickness at the particle location and $Re_d = u_d^* d^*/\nu^*$, where d^* is the diameter of the sphere, ν^* is kinematic viscosity, and, if k^* denotes the height of the top of the sphere above the wall, u_d^* is the velocity of the undisturbed boundary layer flow at k^* (figure 1). Hall (1967) concluded that transition was induced by 'direct seeding' of the turbulent flow in the wedge into the boundary layer and not by inducing linear instability waves. Hall (1967) also observed that when the sphere was moved across the boundary layer in the wall normal direction, turbulent patches developed at Reynolds numbers slightly higher than $(Re_d)_{crit}$ for stationary spheres.

More recently, the effects of stationary spherical particles on the boundary layer were examined in the experiments of Vincent & Petrie (1993). Through flow visualization techniques they investigated the characteristics and structures of the wake leading to the development of the turbulent wedge for both surface-mounted and elevated spheres. For spheres mounted on the wall, the flow field was dominated by the horseshoe and trailing vortex systems observed in previous studies (Mochizuki 1961; Norman 1971; Acarlar & Smith 1987; Klebanoff, Cleveland & Tidstrom 1992). In cases where a turbulent wedge formed, the trailing vortex system rapidly gave way to the shedding of hairpin vortices in the near vicinity of the sphere. As the hairpin vortices were convected downstream, the heads rose upward toward the free stream while the legs descended toward the plate. In the near-wall region, the legs of the hairpin vortices broke down and then the boundary layer became turbulent forming the wedge. The heads of the vortices separated from the legs and developed into isolated vortex rings residing above the turbulent boundary layer. Upon elevating the sphere above the plate, the above scenario outlined for the breakdown of the wake into a turbulent wedge generally did not vary.

In addition to the wake effects outlined above, it has been postulated that surface roughness or particulates can create spatially localized three-dimensional disturbances.

https://doi.org/10.1017/S0022112097006198 Published online by Cambridge University Press

In recent numerical and experimental studies focusing on such localized disturbances, Breuer & Haritonidis (1990), Breuer & Landahl (1990), and Henningson, Lundbladh & Johansson (1993) observed the algebraic temporal growth of disturbances which they describe as the 'lift-up' mechanism (Landahl 1975). For sufficiently high perturbation amplitudes, Breuer & Landahl (1990) observed that the algebraic growth can cause the flow to bypass the linear stability route (Tollmien–Schlichting (T-S) waves, which have exponential growth rates) directly into turbulence. The development of this type of disturbance is characterized by two parts: a wave portion behaving according to linear stability theory, and a transient portion which travels at the local mean velocity. The transient part is associated with the so-called lift-up mechanism (Landahl 1975) which generates horizontal perturbation velocity by the vertical motion of fluid particles in the presence of mean shear. Landahl (1980) determined that the kinetic energy of this type of disturbance grows linearly (or faster) in time as indicated by linear growth of streamwise perturbation velocity, u', and/or streamwise elongation of the disturbance. In the work of Breuer & Haritonidis (1990), it was observed that at low Reynolds numbers or low perturbation amplitudes this growth can dampen and in some cases the transient part decays and only the wave part remains.

In this work, we numerically investigate the mechanisms by which an elevated stationary sphere can induce transition in the boundary layer. As a precursor to this problem, the evolution of an isolated disturbance in the boundary layer is simulated using a spatial numerical model and the results are compared with the temporal computations of Breuer & Landahl (1990) and Henningson *et al.* (1993). The purpose of these computations is to provide reference characteristics of the evolutionary behaviour of isolated disturbances for direct comparison with particle-induced transition and to determine the minimum mesh resolution needed to accurately capture the disturbance behaviour.

The computations involving the sphere in the boundary layer reveal that isolated disturbances are characteristic of particle-induced perturbations, linking transition caused by particles to three-dimensional disturbances. This result is extracted from two simulations which capture sub- and supercritical behaviour of the wake of a sphere in the boundary layer. We also survey the properties of the sphere wake and compare our numerical results with previous experimental observations.

2. Computational method

The numerical model integrates the full three-dimensional time–dependent incompressible Navier–Stokes equations non-dimensionalized by the boundary layer displacement thickness at the inflow, δ_o^*, and free-stream velocity, U_∞, by a time splitting method. The Crank–Nicolson scheme is implemented on the normal diffusion terms and the Adams–Bashforth method is applied on the remaining terms. The equations are discretized on a non-staggered grid by fourth-order central finite differences in the streamwise (x) direction and by the Chebyshev collocation matrix method in the normal (y) direction. The spanwise (z) direction is assumed to be periodic thus enabling the use of Fourier expansions. As we consider spatial growth of disturbances approximating more closely actual laboratory experiments, the inflow and outflow conditions must be properly imposed. To this end, we employ the buffer domain technique for the outflow boundary conditions which ensures smooth passage of disturbance waves out of the computational domain (Streett & Macaraeg 1989; Saiki *et al.* 1993). The pressure Poisson equation is solved by the capacitance matrix

https://doi.org/10.1017/S0022112097006198 Published online by Cambridge University Press

method. Further details of the numerical scheme are given elsewhere (Danabasoglu, Biringen & Streett 1991; Danabasoglu 1992; Joslin, Streett & Chang 1993; Saiki *et al.* 1993).

To simulate the boundary of the sphere in the flow within a Cartesian geometry, we implement a virtual boundary method developed by Goldstein, Handler & Sirovich (1993, 1995) based on the initial work of Sirovich (1967, 1968). This technique involves the imposition of a no-slip boundary in a flow through a feedback forcing function which is added to the momentum equations. The feedback function effectively brings the fluid velocity to zero at the desired points in the flow which define the no-slip boundary. This force can be expressed as (Goldstein *et al.* 1993)

$$\boldsymbol{F}(\boldsymbol{x}_b, t) = \alpha \int_0^t \boldsymbol{U}(\boldsymbol{x}_b, t)\mathrm{d}t + \beta \boldsymbol{U}(\boldsymbol{x}_b, t). \tag{2.1}$$

Here, $\boldsymbol{F}$ is the external force imposed at the desired boundary points defined by $\boldsymbol{x}_b$, and $\boldsymbol{U}$ is the velocity at these surface points. The nature of the expression is such that the velocity field feeds back into the term forcing $\boldsymbol{U}$ to go to zero. The dimensional negative constants, α and β, are determined by observing the response of $\boldsymbol{U}$ once $\boldsymbol{F}$ is applied; α produces the natural oscillation frequency of the response, while β dampens the oscillation of the response. Thus, for unsteady flow, α must produce a response with a natural frequency $((1/2\pi)|\alpha|^{1/2})$ greater than the highest frequencies present in the flow so that $\boldsymbol{F}$ can respond correctly to the changing flow field. Previous test cases (Saiki & Biringen 1996) involving flow around a stationary cylinder clearly reveal that the oscillatory behaviour associated with the virtual boundary does not affect the results by introducing extraneous frequencies. In the test case considering steady-state flow (low Reynolds number), a stationary bubble was obtained which did not 'pulse' or move at any frequency. For unsteady flow (high Reynolds number where vortices are shed), there was no other frequency present in the flow apart from the shedding frequency of the vortices.

The time step for stability in this method depends on α and β as well as the explicit time integration implemented in the flow solver. For the Adams–Bashforth method, Goldstein *et al.* (1993) determined the following expression for the time step:

$$\Delta t < \frac{-\beta - (\beta^2 - 2\alpha k_b)^{1/2}}{\alpha}, \tag{2.2}$$

where k_b is a problem-dependent constant of order one.

A detailed analysis demonstrating characteristics of the virtual boundary method through a series of test cases involving modelling stationary and moving cylinders is given in Saiki (1995) and Saiki & Biringen (1996) and we will refer to the results from these studies as related to the discussion in subsequent Sections.

3. Results: isolated three-dimensional disturbance

In this Section, we discuss numerical simulations investigating the development of an isolated disturbance induced by two pairs of counter-rotating streamwise vortices in the boundary layer. These results demonstrate the capability of the present flow solver to successfully capture the evolution of an isolated three-dimensional disturbance with a spatial computational model and delineate the two-part behaviour of the three-dimensional disturbance. As will be shown in subsequent Sections, such disturbances characterize particle-induced perturbations in the boundary layer.

https://doi.org/10.1017/S0022112097006198 Published online by Cambridge University Press

The inflow conditions introducing the two pairs of streamwise vortices were adapted from the initial conditions implemented by Breuer & Landahl (1990) in their temporal simulations of the evolution of a high-amplitude isolated disturbance. These perturbation conditions are applied at the inflow and are expressed as

$$\left.\begin{aligned} u'(x=0,y,z,t) &= 0, \\ v'(x=0,y,z,t) &= (A_v/l_z)\sqrt{\tfrac{1}{2}}y_v^3(1-2z_v^2)\mathrm{e}^{(-1/2-y_v^2-z_v^2)}\sin(\omega_v t), \\ w'(x=0,y,z,t) &= -(A_v/l_y)\sqrt{\tfrac{1}{2}}z_v(3y_v^2-2y_v^4)\mathrm{e}^{(-1/2-y_v^2-z_v^2)}\sin(\omega_v t). \end{aligned}\right\} \tag{3.1}$$

In the above set of equations, A_v is the amplitude of the vortices, and $y_v = y/l_y$ and $z_v = z/l_z$, where l_y, and l_z are the characteristic normal and spanwise scales of the disturbance. The term $\sin(\omega_v t)$ governs the time evolution and ω_v is adjusted in order to obtain a set of vortices similar in size to those of Breuer & Landahl (1990). These conditions are imposed over one cycle of the sine term only giving rise to two pairs of vortices. Once they have formed, the conditions in (3.1) are no longer imposed.

In this computation adopting the higher-amplitude disturbance case of Breuer & Landahl (1990), the normal and spanwise length scales of the disturbance were defined as $l_y = 1.2$ and $l_z = 6$, and the amplitude of the vortices was $A_v = 0.5$ resulting in maximum inflow perturbation amplitudes of $v_{max} = 5.8\times10^{-3}$ and $w_{max} = 1.86\times10^{-2}$. The computations were performed on several computational grids of varying normal resolution, $241\times61\times33$, $241\times71\times33$, and $241\times101\times33$ in a domain of dimensions $141\times75\times50$ units non-dimensionalized by displacement thickness, δ^*. The Reynolds number specified at the inflow was $Re_{\delta_o^*} = 950$, and the vortex pairs were centred around $z = 25$.

In accordance with Breuer & Landahl's (1990) study, the current computations displayed the development of the transient and wave parts associated with the three-dimensional disturbance. The initial startup of the streamwise vortices can be observed in (x, y)-planes of perturbation velocity contours at the centreline of the streamwise vortices, $z = 25$ (figures 2*a* and 3*a*). The perturbation quantities were obtained by subtracting the base flow (Blasius solution) from the total solution. At this point in the computation, the full cycle of introducing the pairs of streamwise vortices has been completed and the sine term in (3.1) has just been set to zero. The normal perturbation velocity contours (figure 3*a*) reveal that the downstream set of vortices (closest to the outflow) brings low-momentum fluid upward from the wall at the centreline, $z = 25$, while the second set of vortices developing upstream reflects exactly the opposite behaviour. The vertical motion of the fluid induces the production of horizontal velocity (reflected in the u' contours, figure 2*a*) by the lift-up effect, i.e. fluid is moved vertically while retaining its horizontal momentum.

The two-part evolution of the disturbance as it travels downstream is shown in similar (x, y)-planes at $z = 25$ in figures 2(*b–d*) and 3(*b–d*). At this spanwise position the u' contours are dominated by the higher-amplitude transient structure appearing as a negative contour region followed by a positive region which develop in accordance with the vertical motion of the fluid. Since the transient part moves at the local velocity, the presence of mean shear associated with the boundary layer causes the structure to tilt and stretch in the streamwise direction. The original form of the disturbance coupled with the stretching and tilting of the structure leads to the development of an internal shear layer (figure 2*b, c*). The time evolution of the maximum perturbation velocities associated with the transient part reveal that the amplitude of u' increases in a linear fashion from $t \approx 6.5$ to $t \approx 100$.

https://doi.org/10.1017/S0022112097006198 Published online by Cambridge University Press

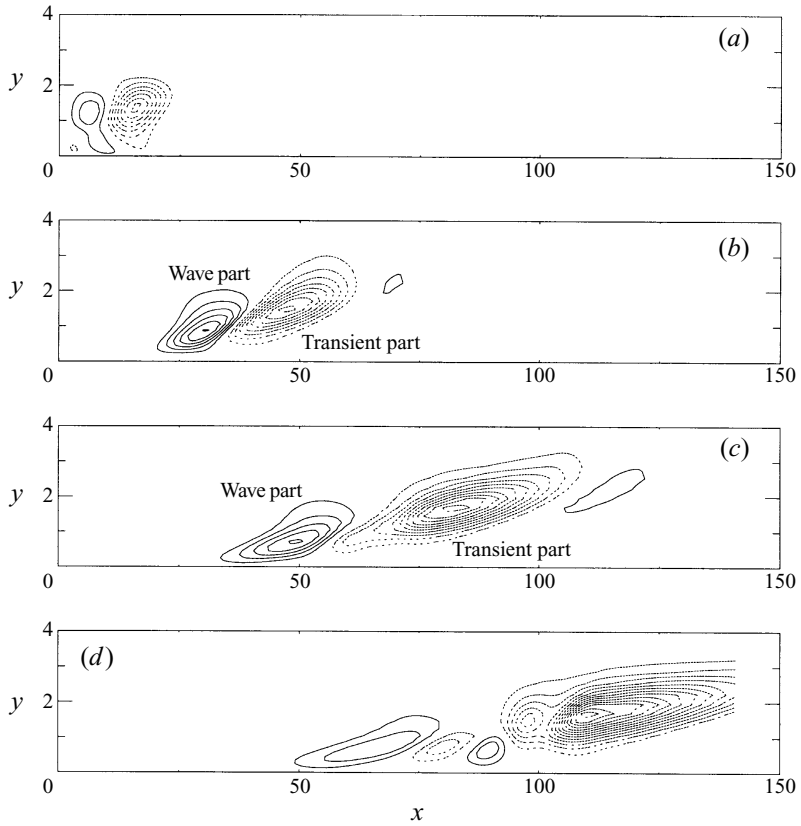


FIGURE 2. Contours of streamwise perturbation velocity in the (x, y)-plane at $z = 25$: (*a*) $t = 32.7$, (*b*) $t = 85.1$, (*c*) $t = 137.44$, and (*d*) $t = 189.8$. In this and the following figures, negative and positive quantities are denoted by ····· and ——— , respectively, and the vertical direction is magnified.

The normal perturbation velocity contours presented in figure 3 clearly reveal the wave part of the disturbance. The contours are similar to those which develop due to the presence of a Tollmien–Schlichting (T-S) wave. The wave part of the disturbance travels at the phase speed of the T-S wave, lagging behind the transient part; the transient part in v' contours is indicated by the negative region of fluid which moves ahead of the wave portion (figure 3*b*, *c*). At $t = 137.44$ (figure 3*c*), a secondary wave indicated by the splitting of the positive v' cell appears which, according to Breuer & Landahl (1990), is associated with a secondary instability.

Recently, Henningson *et al.* (1993) reproduced the Breuer & Landahl (1990) computations summarized above and did not observe this type of behaviour, i.e. secondary instability. They attributed this discrepancy to insufficient resolution in the normal direction in the analysis of Breuer & Landahl (1990). To test their assertion, we performed several calculations with higher normal resolution, increasing the number of points within the boundary layer by changing the stretching near the wall and increasing the number of points in the normal direction. The v' contours obtained for the middle resolution case ($241 \times 71 \times 33$) reveal no development of a secondary wave (figure 4) confirming that the computations performed by Breuer & Landahl (1990) were under resolved. Identical results were obtained in the highest-resolution case, $241 \times 101 \times 33$, demonstrating that the middle resolution results are grid independent and sufficient for capturing the evolution of the three-dimensional disturbance.

https://doi.org/10.1017/S0022112097006198 Published online by Cambridge University Press

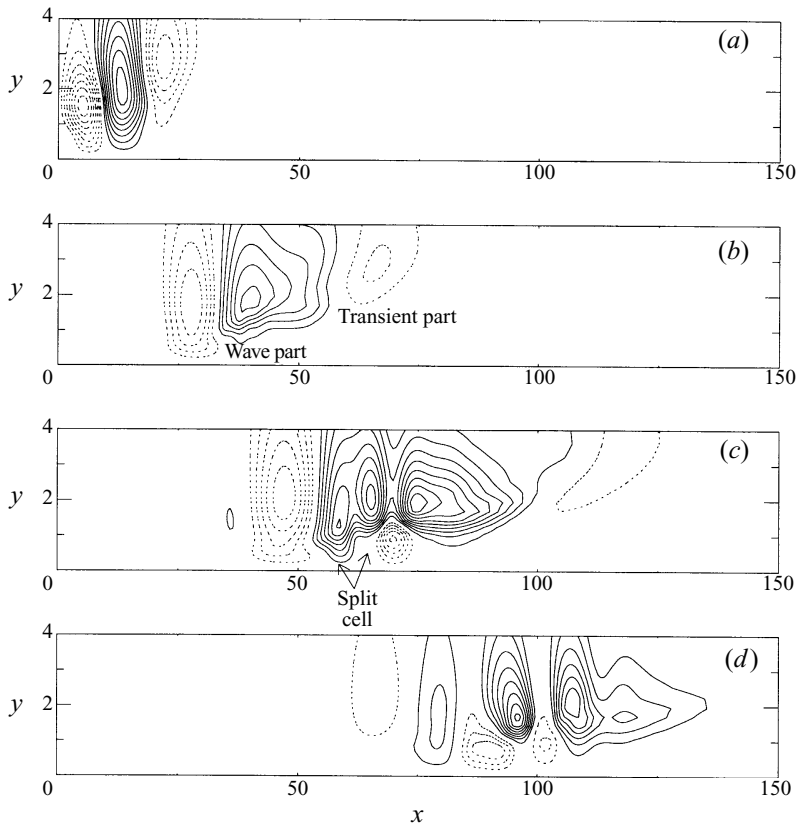


FIGURE 3. Contours of normal perturbation velocity in the (x, y)-plane at $z = 25$: (a) $t = 32.7$, (b) $t = 85.1$, (c) $t = 137.44$, and (d) $t = 189.8$.

These computations allowed us to clarify the issue regarding minimum grid resolution needed to accurately compute the physical behaviour of this type of phenomenon and to compare results obtained from temporal and spatial mathematical models. More importantly, the structure associated with the two-part nature of the isolated disturbance was determined in order to identify such disturbances which arise in the sphere computations presented in the following Sections.

4. Results: effects of a sphere on boundary layer transition

The subcritical and supercritical behaviour of the wake of a sphere in the boundary layer was examined by simulating two cases distinguished by the displacement boundary layer Reynolds numbers applied at the inflow boundary, $Re_{\delta_o^*} = 500$ and $Re_{\delta_o^*} = 750$ (table 1). This parameter, in conjunction with the non-dimensional downstream position of the sphere from the inflow ($x_c = 31.14$) and the height of the top of the sphere from the wall ($k = k^*/\delta_o^* = 1.3$; figure 1), resulted in sphere Reynolds numbers of $Re_d = 322$ and $Re_d = 494$ for the subcritical and supercritical cases, respectively. The sphere was well within the boundary layer at this normal location and the sphere elevation above the plate placed it in Region II according to the criteria of Hall (1967). In this height region, Hall (1967) determined that the critical Re_d for development of a turbulent wedge was between 450 to 700 and Re_d in the

https://doi.org/10.1017/S0022112097006198 Published online by Cambridge University Press

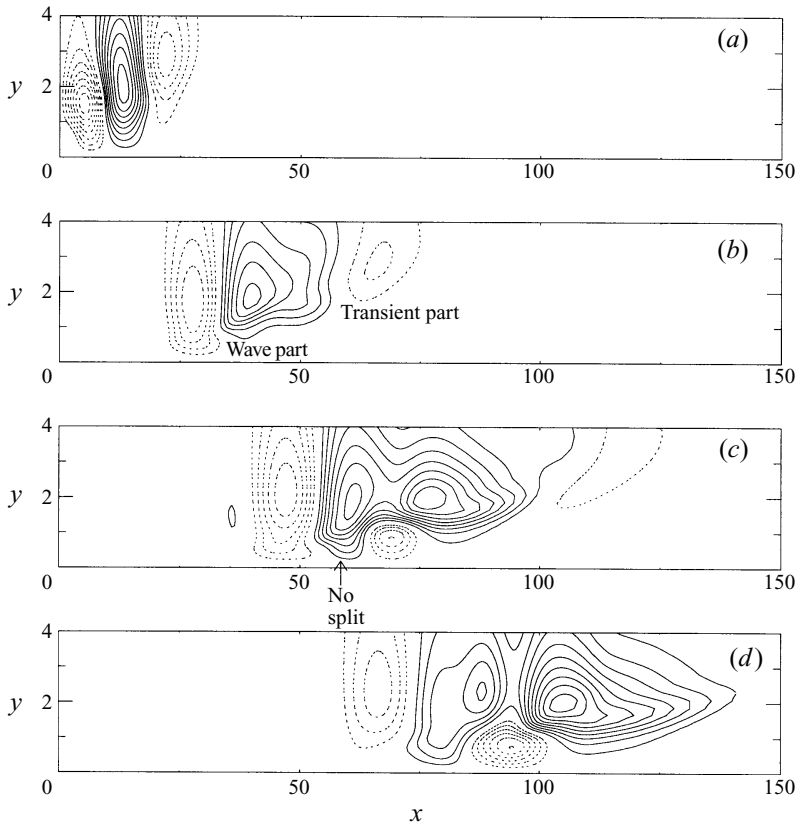


FIGURE 4. High normal resolution case: $241 \times 71 \times 33$. Contours of normal perturbation velocity in the (x, y)-plane at $z = 25$: (*a*) $t = 32.7$, (*b*) $t = 85.1$, (*c*) $t = 137.44$, and (*d*) $t = 189.8$.

Case	$Re_{\delta_o^*}$	Re_d	$Re_{\delta_p^*}$	(x_c, y_c, z_c)	δ_p^*	Mesh resolution	Domain size
Subcritical	500	322	544	$(31.14, 0.8, \pi)$	0.395	$306 \times 71 \times 33$	$137.36 \times 75 \times 2\pi$
Supercritical	750	494	795	$(31.14, 0.8, 2\pi)$	0.4058	$306 \times 71 \times 65$	$137.36 \times 75 \times 4\pi$

TABLE 1. Computational parameters implemented for the sphere cases

subcritical case falls well below this range, while Re_d for the supercritical case lies within 450–750 for supercritical behaviour.

In both computations, the diameter of the sphere was $d^* = 2.297$ mm (roughly, $d^* = \frac{1}{3}\delta_p$; δ_p is the dimensional laminar boundary layer thickness at the sphere position, x_c). The sphere was elevated and its bottom was 0.3 non-dimensional units above the plate. Both computational cases were set up such that the dimensional diameter of the sphere was equal to the boundary layer displacement thickness at the inflow, i.e. $d^* = \delta_o^*$. Recall that the displacement thickness of the boundary layer at the inflow boundary is chosen as the characteristic length non-dimensionalizing the governing equations, therefore the non-dimensional diameter of the sphere in the current computations was equal to one.

The selection of the position of the sphere was based upon the parameters implemented in the experimental studies of Blackwelder *et al.* (1992). In particular, the

https://doi.org/10.1017/S0022112097006198 Published online by Cambridge University Press

streamwise location of the sphere in the subcritical case corresponded to the location where the particle struck the plate and then induced a turbulent spot in the median Reynolds numbers ($Re_x = 1 \times 10^5$) cases examined by R. Blackwelder & P. Tanaguichi (personal communication). The height of the sphere above the plate was chosen in order to obtain the best resolution for defining the sphere with the virtual boundary method and by requiring that the sphere was within one boundary layer thickness of the wall. Owing to the imposition of periodicity in the spanwise direction, the simulations model the flow over an infinite array of spheres where the distance between the spheres was $5.28d^*$ and $11.56d^*$ for the sub- and supercritical cases, respectively.

The boundary of the sphere was imposed by the forcing term applied on 368 points with feedback coefficients set to $\alpha = -500$ and $\beta = -4$. The virtual boundary method requires point by point enforcement of the forcing term on the grid points, thus to approximate the shape of the sphere as closely as possible, additional mesh points in the streamwise direction were clustered in the vicinity of the sphere. As required by the virtual boundary method, the natural frequency of the forcing term, $(1/2\pi)|\alpha|^{1/2} = 3.6$, exceeded the maximum frequencies which developed in both cases. The vortex shedding frequencies of the hairpin vortices were 0.2 and 0.22 in the sub- and supercritical case, respectively and in the incipient turbulent wedge of the high Reynolds number case, the maximum frequencies measured were less than one. The body of the sphere was introduced by 'turning on' the forcing term at $t = 0$ within a Blasius boundary layer. Previous studies (Goldstein *et al.* 1993; Saiki & Biringen 1996) have demonstrated that this method of introducing the virtual boundary results in the quick formation of the body such that time-accurate development of the flow around the body can be obtained. For example, computations by Saiki & Biringen (1996) of the time-dependent evolution of the wake downstream of a rotating cylinder revealed excellent agreement with experimental observations.

4.1. *Subcritical case*

For this computation, a mesh of $306 \times 71 \times 33$ was defined on a physical domain of dimensions $137.36 \times 75 \times 2\pi$. The length of the buffer domain was 62.64 non-dimensional lengths, comprising 116 grid points. The code utilized the maximum time step allowable which obeys the Courant and virtual boundary method restrictions and was set to $\Delta t = 0.0224$. The non-dimensional coordinates of the centre of the sphere were $(x_c, y_c, z_c) = (31.14, .8, \pi)$, and the height of top of the sphere was $k^*/\delta_p = 0.395$. The sphere Reynolds number was $Re_d = 322$ and the Reynolds number based on the laminar boundary layer displacement thickness at the sphere location was $Re_{\delta_p^*} = 544$.

The wake of the sphere in the subcritical case is composed of four physical regions which develop over a range of streamwise locations downstream of the sphere: (i) the flow field arising in the immediate vicinity of the sphere consisting of two separation bubbles, one attached to the wall and the other to the downstream side of the sphere ($0 \leqslant \overline{x} \leqslant 2.8$), (ii) a pair of fixed trailing vortices extending downstream of the sphere ($0 \leqslant \overline{x} \leqslant 6$), (iii) a hairpin vortex shedding region where the hairpins are the strongest before decaying downstream ($6 \leqslant \overline{x} \leqslant 24$), and (iv) the region downstream where the hairpin vortices dissipate ($24 \leqslant \overline{x} \leqslant 106$). Here, we denote $\overline{x}$ as $\overline{x} = x - x_d$ where x_d is the streamwise location of the downstream edge of the sphere. These regions will be referred to in the subsequent discussion.

https://doi.org/10.1017/S0022112097006198 Published online by Cambridge University Press

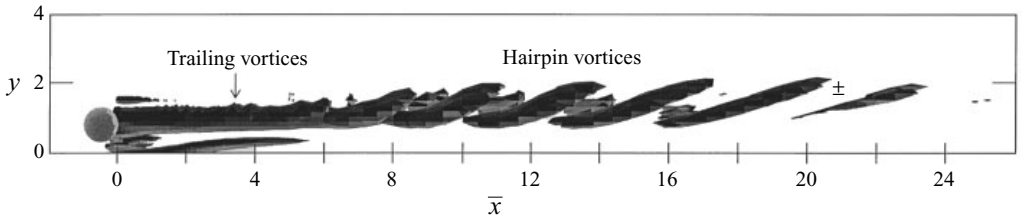


FIGURE 5. Subcritical case: side view of isosurfaces of streamwise vorticity. The levels are ± 0.1.

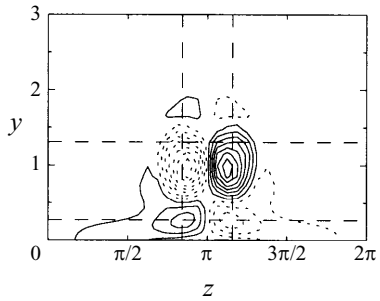


FIGURE 6. Subcritical case: contours of streamwise vorticity in (z, y)-planes at $\bar{x} = 3.5$. In this and the following figure, the negative and positive regions are denoted by ····· and ——— , respectively, and the boundaries of the sphere are marked by — — — . The flow direction is into the page.

4.1.1. *Trailing and hairpin vortices*

The flow field settles into a quasi-steady state consisting of hairpin vortices shed into the wake. This is clearly demonstrated in figure 5 where a side view of instantaneous streamwise vorticity isosurfaces demarcate the legs of six hairpin vortices in the near-sphere region spanning $0 \leqslant \bar{x} \leqslant 27$. The hairpin heads are absent in isosurfaces of streamwise vorticity, because they consist mainly of spanwise vorticity; however, the rise of the heads of the vortices towards the free stream is clearly indicated by the vortex legs. The shed vortices ultimately dissipate as they are convected downstream and the flow returns to its laminar boundary layer state. This behaviour is in good agreement with experimental results; for subcritical Reynolds numbers Mochizuki (1961), Hall (1967), and Vincent & Petrie (1993) observed laminar shedding of vortices.

The motion of the pair of trailing streamwise vortices as revealed in cross-planes of streamwise vorticity contours at $\bar{x} = 3.5$ (figure 6) moves low-momentum fluid away from the wall at the centreline of the wake, $z = \pi$, which interacts with higher-speed fluid above and transfers high-speed fluid toward the wall at the outer bounds of the vortices. Further downstream, this self-induced motion causes the vortices to approach each other and to rise slightly towards the free stream. At about six diameters downstream of the sphere, the hairpin vortex shedding commences.

The hairpin vortex structure and development are in accordance with observations obtained by experimental studies of hairpin vortices (Acarlar & Smith 1987). Cross-planes of streamwise vorticity at $\bar{x} = 6.8$ and 8.1 (figure 7) show that the motion of the legs exhibit the same direction of rotation as the trailing vortices described above, thus inducing the same fluid motion as the trailing vortices. The self-induced motion of the vortices results in the head of the vortex lifting upward toward the free stream allowing higher velocities to carry the head downstream faster than the

https://doi.org/10.1017/S0022112097006198 Published online by Cambridge University Press

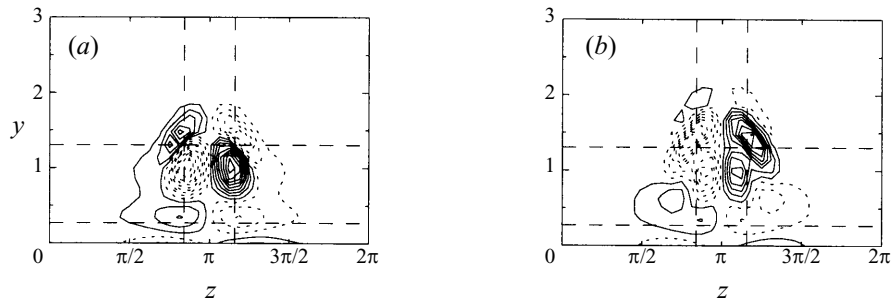


FIGURE 7. Subcritical case: contours of streamwise vorticity in (z, y)-planes at (a) $\overline{x} = 6.8$, and (b) $\overline{x} = 8.1$.

legs. This action leads to a stretching of the legs as the hairpin vortices are convected downstream (figure 5). The legs of the hairpin vortex initially form an angle of 25° with the wall which is slightly lower than the angle measurement of 30°–35° observed by experiments for elevated spheres (Vincent & Petrie 1993); further downstream as the legs are stretched, the angle decreases. The legs extend towards the plate to a level near the midpoint of the sphere ($y \approx 0.734$), but they do not descend any further towards the wall. The maximum height to which the hairpin vortices rise is $y \approx 2.3$ or $y/\delta_p \approx 0.7$ which is well within the boundary layer. This behaviour is in agreement with Vincent & Petrie (1993) who observed that the hairpin vortices did not lift up into the free stream for Reynolds numbers $Re_d \leqslant 480$–500. Figures 5 and 7(b) also reveal that the upstream portion of the hairpin vortex legs appears to be intertwined with the legs of the newer vortex similar to the flow visualization results of Acarlar & Smith (1987).

Evidence of the hairpin eddy structure can be identified by observing time traces at various y and z locations of streamwise velocity in the hairpin vortex region. Experimental studies have observed that the configuration of a hairpin eddy is associated with a phase reversal in the time signal with increasing normal direction above the hairpin vortex and outward from the centreline (Klebanoff, Cleveland & Tidstrom 1962; Klebanoff *et al.* 1992). This behaviour in the normal direction is demonstrated in figure 8(a, b) where distributions over four vortex shedding periods at $\overline{x} = 10.6$ and $z = \pi$ for $y = 2.8$ and 1.3 are presented. The height of the vortex which passes through this streamwise location is $y = 1.86$ and the normal locations of the time traces shown in figure 8(a, b) span this height. The maxima in the time distribution above the vortex (figure 8a) correspond to the passage of each hairpin head; the vortical motion of the head creates an increase in streamwise velocity above it and a deficit below it. Accordingly, the time signal at $y = 1.3$ (figure 8b) reveals minima associated with the passage of the heads. The minima appearing in the distribution above the vortices is associated with the motion of the hairpin legs moving low-momentum fluid up toward the free stream. The phase change between time signals recorded at the centreline and spanwise positions at the outer extremities of the hairpin vortex is demonstrated by a comparison of figures 8(b) and 8(c). The distributions off the centreline display minima and maxima due to the vortical motion of the hairpin vortex moving high-momentum fluid from the free stream toward the wall at the outer spanwise boundaries of the structure. The phase reversals in the spanwise direction begin to develop within one diameter of the sphere measured from

https://doi.org/10.1017/S0022112097006198 Published online by Cambridge University Press

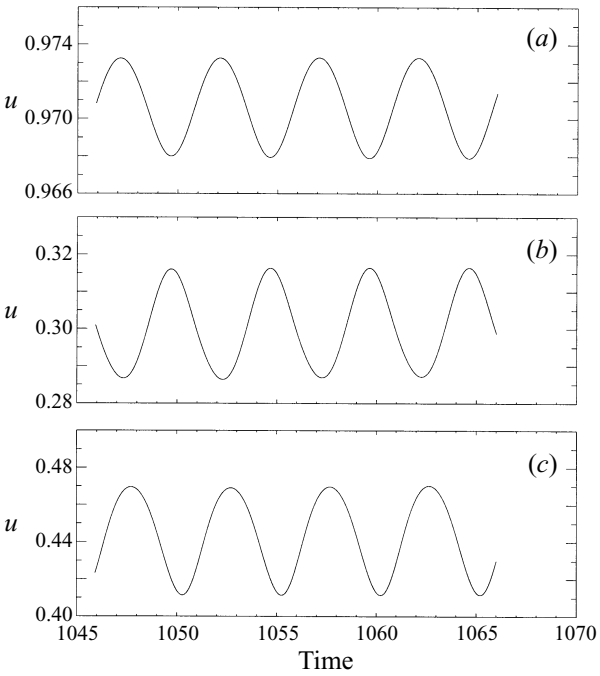


FIGURE 8. Subcritical case: time evolution of streamwise velocity over four vortex shedding periods at $\overline{x} = 10.6$ and (*a*) $y = 2.83$, $z = \pi$, (*b*) $y = 1.3$, $z = \pi$, and (*c*) $y = 1.3$, $z = 2.55$.

$z = \pi$ in a manner similar to time signals measured in the wake of a hemisphere in the boundary layer (Klebanoff *et al.* 1992).

4.1.2. *Boundary layer characteristics*

To assess the effects of the sphere wake on the characteristics of a laminar boundary layer, the non-dimensional displacement thickness ($\overline{\delta}^* = \delta^*/\delta_o^*$), momentum thickness ($\theta$), and skin friction coefficient (c_f) were computed and compared with standard values obtained for the Blasius boundary layer solution. These quantities are determined by the following equations:

$$\overline{\delta}^* = \int_0^{y_{max}} \left(1 - \frac{u_m}{U_\infty}\right) \mathrm{d}y, \tag{4.1}$$

$$\theta = \int_0^{y_{max}} \frac{u_m}{U_\infty}\left(1 - \frac{u_m}{U_\infty}\right) \mathrm{d}y, \tag{4.2}$$

and

$$c_f = \frac{2}{Re_{\delta_o^*}} \left(\frac{\partial u_m}{\partial y}\right)_{y=0}, \tag{4.3}$$

using mean velocity profiles (u_m) computed at the centreline, $z = \pi$. The streamwise mean velocity, u_m, is defined as

$$u_m(x, y, z) = \frac{1}{N_t} \sum_{n=1}^{N_t} u(x, y, z, n\Delta t), \tag{4.4}$$

https://doi.org/10.1017/S0022112097006198 Published online by Cambridge University Press

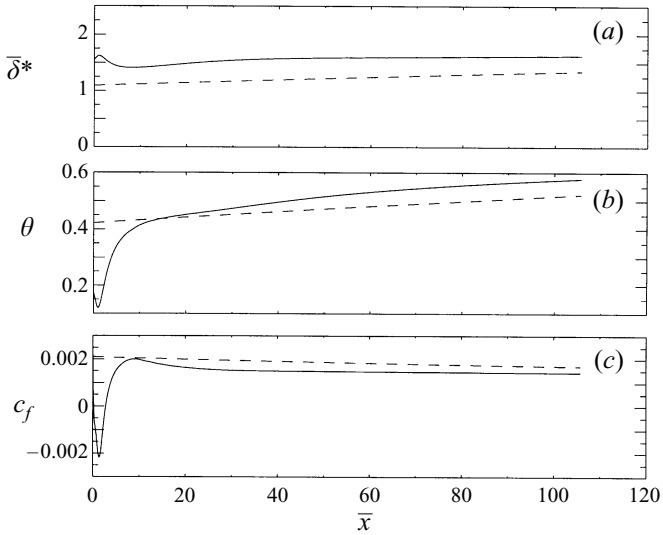


FIGURE 9. Subcritical case: streamwise distribution of (*a*) non-dimensional boundary layer displacement thickness, $\overline{\delta}^*$, (*b*) momentum thickness, θ, and (*c*) skin friction coefficient, c_f, downstream of the sphere. ——— , current solution; and — — — , laminar boundary layer solution.

where Δt is the time step and N_t is the number of time steps. We focus on quantities at the centreline, because the deviation from the laminar boundary layer is the greatest due to the presence of the sphere at that location.

Figure 9 presents the streamwise distribution of $\overline{\delta}^*$, θ, and c_f downstream of the sphere. In the vicinity of the sphere, there is an increase in displacement thickness and a decrease in momentum thickness due to the effects of the body (figure 9*a, b*). This trend continues throughout the region where the separation bubble develops, thus leading to an increase in the shape factor, $H = \overline{\delta}^*/\theta$. The skin friction in this region attains a large negative value characteristic of separated flow; the curve crosses zero at the end of the wall separation bubble at $\overline{x} \approx 2.8$ (figure 9*c*). Beyond the separated region, $\overline{\delta}^*$ and θ begin to decrease and increase respectively, for a short distance. Further downstream $\overline{\delta}^*$ approaches a constant value of 1.6, indicating an increase in boundary layer displacement thickness over the laminar value of 1.35 due to the wake of the sphere. The momentum thickness remains below the laminar boundary layer value downstream of the separated region, and this behaviour, coupled with the higher $\overline{\delta}^*$, results in a larger shape factor, $H = 2.8$; the value of H for the Blasius boundary layer is ≈ 2.6. The skin friction coefficient remains lower than the Blasius value, indicating that the velocity profiles are less full (δ_u/δ_y at the wall decreases).

4.1.3. *Velocity profiles*

We further characterized the wake of the sphere by examining normal and spanwise profiles of streamwise mean and root-mean-square velocities at $z = \pi$ and various $\overline{x}$ locations. The streamwise component of root-mean-square velocity is defined as

$$u_{rms}(x, y, z) = \left(\frac{1}{N_T} \sum_{n=1}^{N_t} (u(x, y, z, n\Delta t) - u_m(x, y, z)) \right)^{1/2}, \tag{4.5}$$

https://doi.org/10.1017/S0022112097006198 Published online by Cambridge University Press

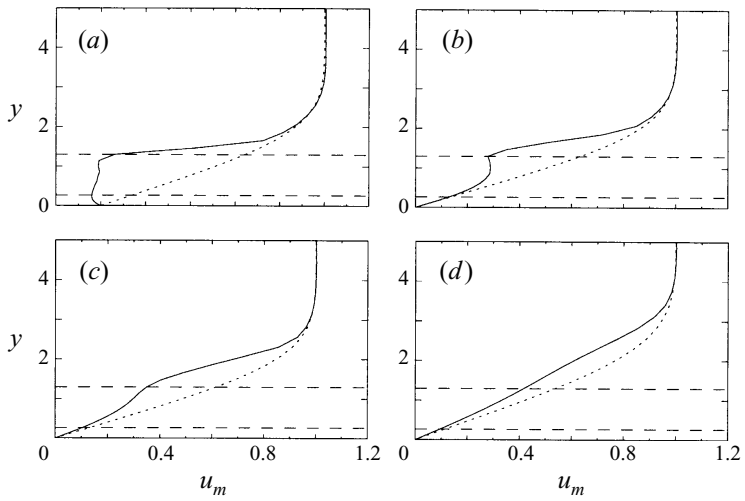


FIGURE 10. Subcritical case: normal profiles of streamwise mean velocity at $z = \pi$. (*a*) $\overline{x} = 1$, (*b*) $\overline{x} = 9$, (*c*) $\overline{x} = 21.44$, and (*d*) $\overline{x} = 102.5$; ——— , streamwise mean velocity; ·····, Blasius profile; — — — , normal boundary of the sphere.

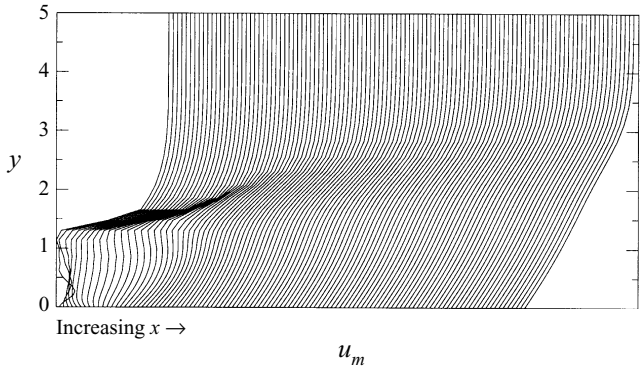


FIGURE 11. Subcritical case: normal profiles of streamwise mean velocity at every other streamwise location downstream of the sphere at $z = \pi$. Each profile is offset by $\Delta u = 0.02$.

where u_m is the streamwise mean velocity as defined in (4.4). Each normal mean profile is compared with the Blasius solution and the locations of the sphere in the computation are denoted by dashed lines. The presence of a separation bubble attached to the wall in the near vicinity of the sphere is reflected in the mean profile at $\overline{x} = 1$ by a small region of reverse flow which extends from the wall to $y \approx 1$ (figure 10*a*). A slight negative bump in the profile near $y \approx 1.25$ indicates the presence of the separation bubble attached to the sphere. The profiles are highly inflectional at the top of the sphere due to the formation of a high-shear layer (figure 10*b*, *c*). This high-shear layer is further evident in figure 11 where streamwise mean velocity profiles at every other $\overline{x}$ location downstream of the sphere at $z = \pi$ are presented. In this figure, the profiles are offset from each other by $\Delta u = 0.02$ in order to observe the shear layer moving away from the wall in association with the rising motion of the hairpin vortices. This behaviour is also reflected in the mean velocity profiles in figure 10*b*, *c* as the inflection points of the profiles move away from the wall and the deviation of the distributions from the Blasius profile is confined to higher normal

https://doi.org/10.1017/S0022112097006198 Published online by Cambridge University Press

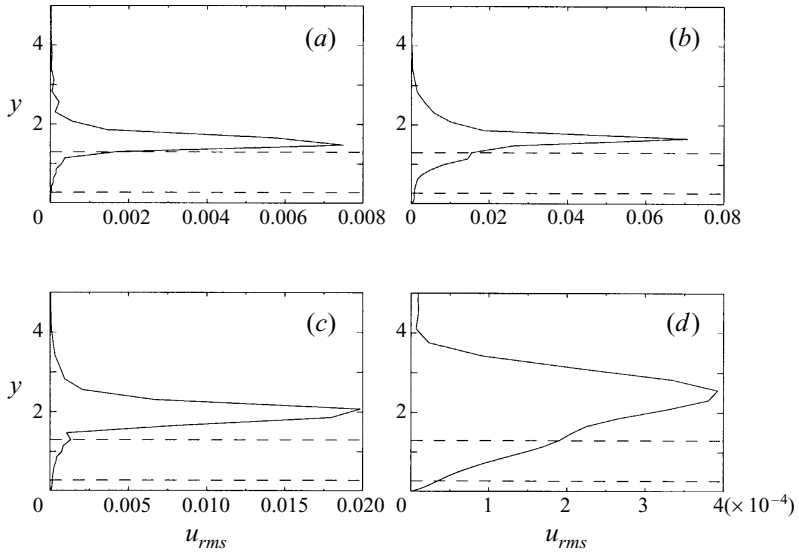


FIGURE 12. Subcritical case: normal profiles of streamwise root-mean-square velocity at $z = \pi$. (*a*) $\overline{x} = 1$, (*b*) $\overline{x} = 9$, (*c*) $\overline{x} = 21.44$, and (*d*) $\overline{x} = 102.5$; ——— , streamwise r.m.s. velocity; — — — , normal boundary of the sphere.

locations above the wall. The effects of the sphere have not completely diminished by the end of the computational domain and there is still some difference between the mean computational profiles and the Blasius profiles (figure 10*d*).

The most striking characteristic of the root-mean-square profiles presented in figure 12 is the appearance of distinct maxima near the top of the sphere which correspond to the inflection point of the mean profiles. The normal position of the maxima migrates away from the wall in accordance with the mean profile inflection point (figure 12*b, c*). Experimental studies have shown the appearance of this high-intensity peak related to the heads of the hairpin vortices in similar profiles (Acarlar & Smith 1987; Vincent & Petrie 1993; Klebanoff *et al.* 1992). Further downstream low-level fluctuations of the profiles due to the wake of the sphere reveal fuller r.m.s. profiles with the maxima developing well above the top of the sphere (figure 12*d*).

Note that the appearance of the inflection points in the mean profiles does not act as a precursor to turbulence for the subcritical sphere Reynolds number case. While the perturbations are greatest at or above the inflection points they do not amplify, but rather attenuate further downstream. As stated by Morkovin (1985), the presence of the sphere allows the development of inflectional profiles without appearing to enhance the linear instability of the flow. This is in part due to the time and length mismatch between the disturbances introduced into the flow field by the hairpin vortices and typical Tollmien–Schlichting waves associated with linear instability. The spatial wavelengths of the disturbances induced by the hairpins are $O(\delta)$ whereas T-S disturbances have much longer wavelengths $O(10\delta)$.

Figure 13 examines spanwise distributions of streamwise mean velocity at several normal locations, $y = 2.82,\ 2.3,\ 1.86,\ 1.3$ (at the top of the sphere), 0.734 (near the y centreline of the sphere), and 0.27 (at the bottom of the sphere) at $\overline{x} = 1$, $\overline{x} = 9$, $\overline{x} = 21.44$, and $\overline{x} = 102.5$. The most obvious characteristic of the mean profiles is the development of a deficit at $z = \pi$ near the top of the sphere due to the motion of

https://doi.org/10.1017/S0022112097006198 Published online by Cambridge University Press

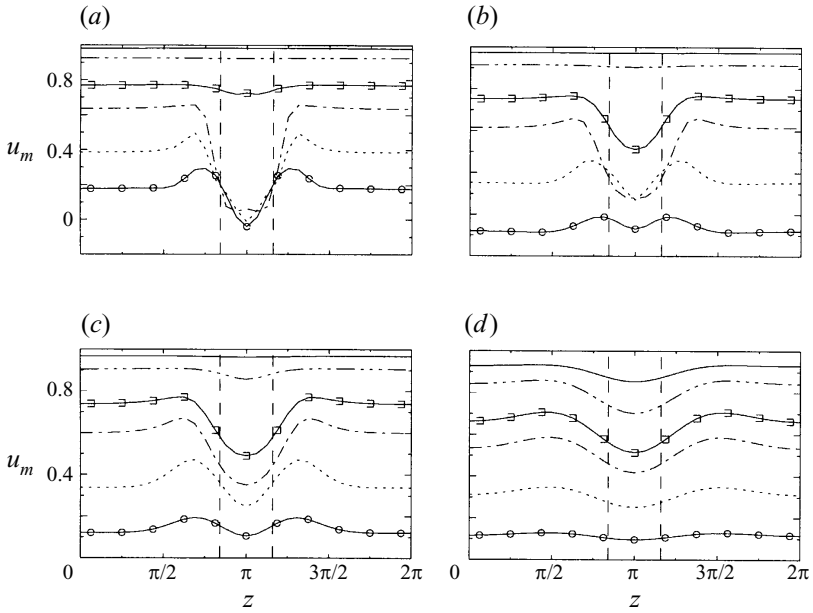


FIGURE 13. Subcritical case: spanwise profiles of streamwise mean velocity at (*a*) $\overline{x} = 1$, (*b*) $\overline{x} = 9$, (*c*) $\overline{x} = 21.44$, and (*d*) $\overline{x} = 102.5$. The normal locations are denoted by ——— , $y = 2.83$; — ··· —, $y = 2.3$; ⊟⊟⊟, $y = 1.86$; — · — , $y = 1.3$; ····· , $y = 0.734$; and o—o—o, $y = 0.27$. The spanwise boundary of the sphere is denoted by — — — .

the trailing streamwise vortices and the hairpin vortices which carry low-momentum fluid away from the wall towards the free stream (figure 13).

4.1.4. *Time evolution and fourier analysis*

To investigate the prominent frequencies/wavenumbers in the flow field, the streamwise velocity field was Fourier transformed in time and in the spanwise direction forming the Fourier amplitudes in the frequency/wavenumber space. Here, we denote these modes as (f, k_z) pairs, where f is non-dimensional frequency ($\omega = 2\pi f$) and k_z is spanwise wavenumber. The streamwise variation of the highest-amplitude modes downstream of the sphere are presented in figure 14. The lowest spanwise modes, $(0, 1)$ and $(0, 2)$, have the highest amplitude throughout the domain with a slight decay with increasing $\overline{x}$. These modes represent the presence of the streamwise trailing vortices in the near vicinity of the sphere and the wake further downstream. The amplitude of the $(0.2, 0)$ mode frequency exhibits a large increase throughout the trailing and hairpin vortex region followed by a dramatic decrease downstream. This mode corresponds to the shedding frequency of the hairpin vortices and, accordingly, Fourier spectra of the time signals in this area reveal a dominant peak at a Strouhal frequency of $St = f^* d^* / U_\infty^* = 0.2$. This result is in good agreement with results extrapolated from the experimental measurements of Vincent & Petrie (1993) for a surface-mounted sphere ($St = 0.19$ at $Re_d = 322$). A second dominant frequency, $(0.017, 0)$, also appears in figure 14 which exhibits similar behaviour to the $(0.2, 0)$ mode near the sphere. However, the lower-frequency mode remains at higher amplitudes than the vortex shedding mode further downstream.

The presence of a second dominant frequency further revealed itself in time series and Fourier analysis of the streamwise velocity. Near the end of the hairpin vortex

https://doi.org/10.1017/S0022112097006198 Published online by Cambridge University Press

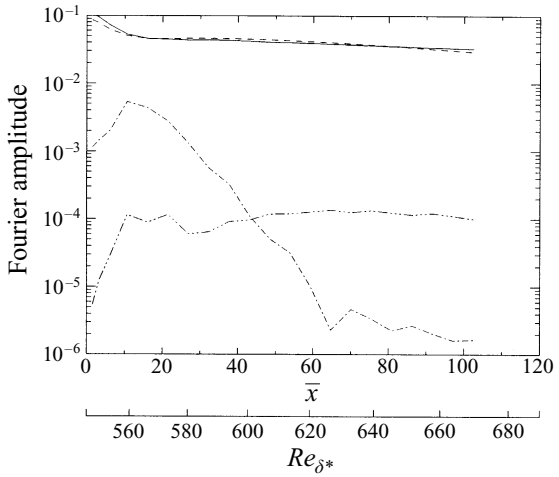


FIGURE 14. Subcritical case: streamwise distribution of Fourier amplitudes of dominant frequency/wavenumber pairs, (f, k_z). ——— , $(0,1)$; — — — , $(0,2)$; –·–·–, $(0.2,0)$; –···–···, $(0.017,0)$. The second horizontal axis indicates the behaviour of these modes with respect to the local boundary-layer displacement thickness Reynolds number, Re_{δ^*}.

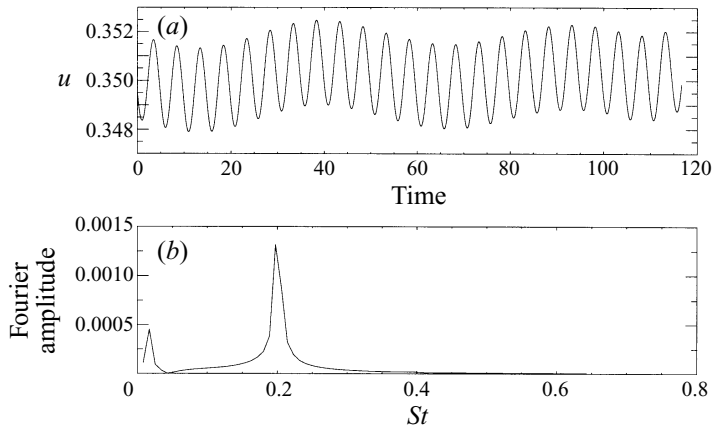


FIGURE 15. Subcritical case: (*a*) time evolution of streamwise velocity over twenty-four vortex shedding periods and (*b*) Fourier spectrum of streamwise velocity vs. Strouhal number at $\overline{x} = 21.44$, $y = 1.3$, and $z = \pi$.

shedding region ($\overline{x} = 21.44$), the second signal manifests itself as a modulation of the shedding signal and as a second spike in the Fourier spectrum (figure 15). The frequency of this signal, $f_l = 0.017$ (or $\omega_l = 0.107$), is not a subharmonic of the shedding frequency, but is less by a factor of ≈ 11.7. Traces of streamwise velocity at points further downstream ($\overline{x} = 48.45$) reveal that the low-frequency signal overshadows the vortex shedding signal and then dominates the flow field completely (figure 16). Moreover, the amplitude of the wave attenuates exponentially in time.

One interesting characteristic of this low-frequency signal is that it appears to be related to the most unstable T-S wave predicted by linear stability theory for the given Reynolds number range of the computational domain. This was confirmed by consultating the stability chart obtained from solutions of the Orr–Sommerfeld equation for the boundary layer and correlating the properly scaled frequency and Reynolds num-

https://doi.org/10.1017/S0022112097006198 Published online by Cambridge University Press

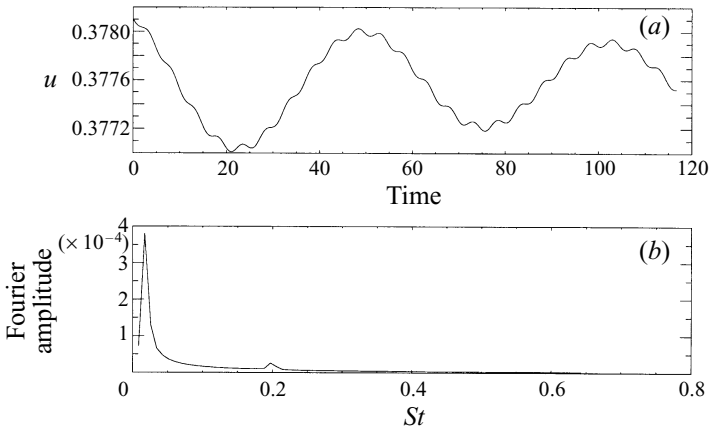


FIGURE 16. Subcritical case: as in figure 15, but at $\overline{x} = 48.45$.

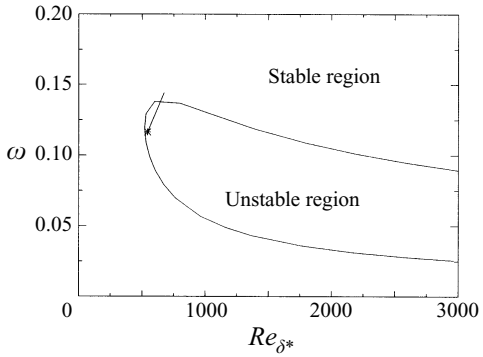


FIGURE 17. Neutral curve (Jordinson 1970) predicted by linear stability theory (solution of the Orr–Sommerfeld equation) for boundary layers; frequency non-dimensionalized by δ^* (ω) vs. Reynolds number (Re_{δ^*}). The region spanned in the subcritical case from the position of the sphere to the end of the domain with respect to the low frequency is denoted by the solid line. The position of the sphere is indicated by $*$.

ber based upon local displacement thickness at the sphere position, $Re_{\delta_p^*} = 544$. For reference, the neutral stability curve for boundary layers as determined by Jordinson (1970) is reproduced in figure 17. In this figure, the region of interest for the current study is denoted by a line drawn from the Reynolds number at the sphere position, $Re_{\delta_p^*} = 544$, to the Reynolds number at the end of the computational domain, $Re_{\delta^*} = 673$, for the low frequency, $\omega_l = 0.107$. According to figure 17, a wave at this frequency experiences growth in the streamwise direction over the majority of the domain; further downstream the wave exhibits a decay in amplitude. This behaviour is reflected in the streamwise distribution of the low-frequency wave amplitude (with some modulation due to the wake of the sphere) shown in figure 14. The second horizontal axis included in figure 14 shows the direct correspondence of the $\overline{x}$-coordinate with the local Reynolds number for comparison with figure 17. The stability chart further reveals that ω_l falls near the frequency of the most unstable wave for the Reynolds number at the location of the sphere, $Re_{\delta_p^*} = 544$ (marked by the asterisk in figure 17). Thus, the low-frequency signal is associated with the appearance of a Tollmien–Schlichting wave, but its origin and the reasons for its time decay require further discussion.

https://doi.org/10.1017/S0022112097006198 Published online by Cambridge University Press

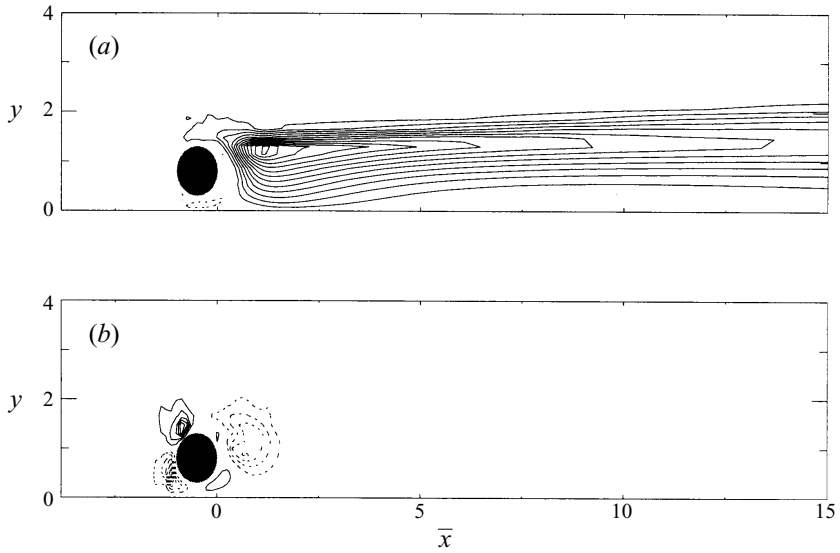


FIGURE 18. Subcritical case: contours of the disturbance at $t = 2.24$. (*a*) Streamwise perturbation velocity and (*b*) normal velocity contours in the $(\overline{x}, y)$-plane at $z = \pi$. In this and following figures, negative and positive quantities are denoted by ····· and ——— , respectively, and the vertical direction is magnified.

The time decay suggests that the source inducing the low-frequency wave is no longer present and is associated with early events of the simulation. This can be related to the initial interaction of the sphere with the boundary layer creating an isolated three-dimensional disturbance which convects downstream ahead of the developing trailing streamwise and hairpin vortices. As noted in the introduction, previous studies have observed that an isolated three-dimensional disturbance in the boundary layer is characterized by two parts: a transient part and a wave part whose behaviour is governed by the lift-up mechanism and by linear stability theory, respectively.

Expanding this idea, contours of streamwise and normal perturbation velocities in the $(\overline{x}, y)$-planes at $z = \pi$ and $z = 2\pi$ detailing the initiation and evolution of the disturbance are presented in figures 18–20. The perturbation quantities (u', v', w') are defined as

$$\boldsymbol{U}'(u', v', w') = \boldsymbol{U}(u, v, w) - \boldsymbol{U}_m(u_m, v_m, w_m), \tag{4.6}$$

where $\boldsymbol{U}_m$ is the mean velocity as defined in (4.4). The mean velocities were computed over 22 periods of the hairpin vortex shedding once the computation reached a quasi-steady state consisting of the hairpin vortices and the final state of the wake. The mean streamwise velocity field reflects the velocity deficit associated with the wake which influences the flow field at distances far from the sphere. Therefore in our analysis, the streamwise perturbation velocities computed by (4.6) are influenced by the wake deficit downstream and significant disturbances are represented by extrema in the u' contour plots.

In the initial stages of the computation, the total normal velocity contours (figure 18*b*) are similar to the flow field which arises around a sphere in uniform flow at low Reynolds numbers. The negative velocity region appearing downstream near the top of the sphere brings high-speed fluid downward forming a region of higher-momentum fluid. This behaviour is revealed in streamwise perturbation velocity

https://doi.org/10.1017/S0022112097006198 Published online by Cambridge University Press

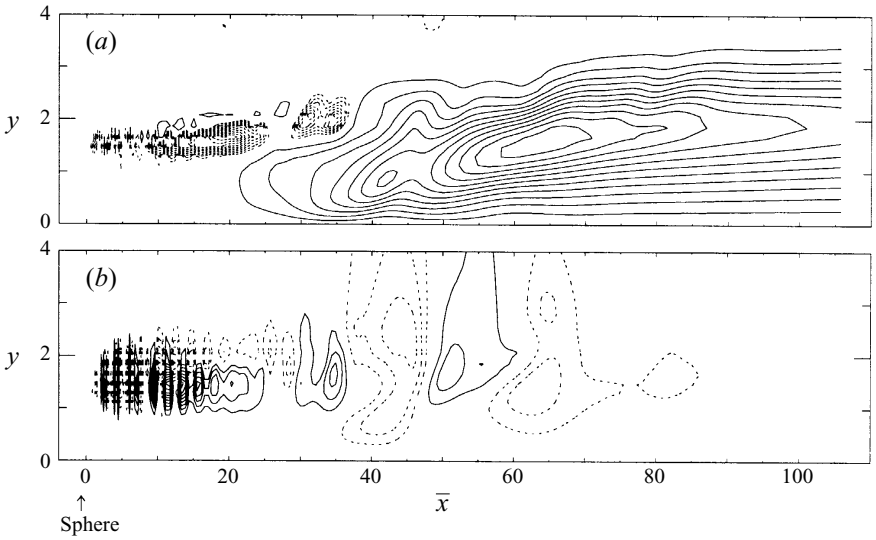


FIGURE 19. Subcritical case: contours of the disturbance at $t = 104.35$. (*a*) Streamwise and (*b*) normal perturbation velocity contours in the $(\overline{x}, y)$-plane at $z = \pi$.

contours, u', where a maximum appears in accordance with the negative-velocity region (figure 18*a*). The origin of the disturbance is associated with the downward motion of fluid, which maintains its horizontal momentum in the presence of mean shear.

The characteristics of the development of the disturbance are similar to those observed in the current study (§ 3) and others (Breuer & Haritonidis 1990; Henningson *et al.* 1993) for an isolated three-dimensional disturbance induced by two pairs of streamwise vortices. Contours of streamwise and normal perturbation velocities in the $(\overline{x}, y)$-planes at $z = \pi$ and $z = 2\pi$ detail the two-part structure of the disturbance at a later time in the computation (figures 19 and 20). The transient portion indicated by the largest maximum in the streamwise perturbation velocity contours at $z = \pi$ (figure 19*a*) is convected downstream at the local velocity of the flow field. The amplitudes associated with the transient part decay; however, the streamwise length of the disturbance increases. The second maximum appearing in the u' contours (figure 19*a*) corresponds to the wave part of the disturbance developing upstream of the transient part. The wave part can be observed in a clearer manner in the $(\overline{x}, y)$-plane away from the centreline at $z = 2\pi$ (figure 20*a*) where the u' contours reveal a distribution similar to those obtained for a T-S wave.

The dominance of the wave part of the disturbance is apparent in the side view of the v' contours at both the centreline, $z = \pi$ (figure 19*b*), and the edge of the domain, $z = 2\pi$ (figure 20*b*). The only indication of the transient part in the v' contours of these figures is the weak negative contours moving out ahead of the wave part. The wave portion travels at a speed estimated as ≈ 0.4, which is slower than the transient portion. Note that the phase speed of the most unstable T-S wave associated with the low frequency ($\omega_l = 0.107$) is 0.39 (according to linear stability theory) in good agreement with the speed of the wave part of the disturbance. Thus, the dispersive part of the disturbance is the source of the decaying low-frequency signal dominating the flow field away from the sphere. Further downstream, the transient portion convects away ahead of the wave part, and in the quasi-steady state

https://doi.org/10.1017/S0022112097006198 Published online by Cambridge University Press

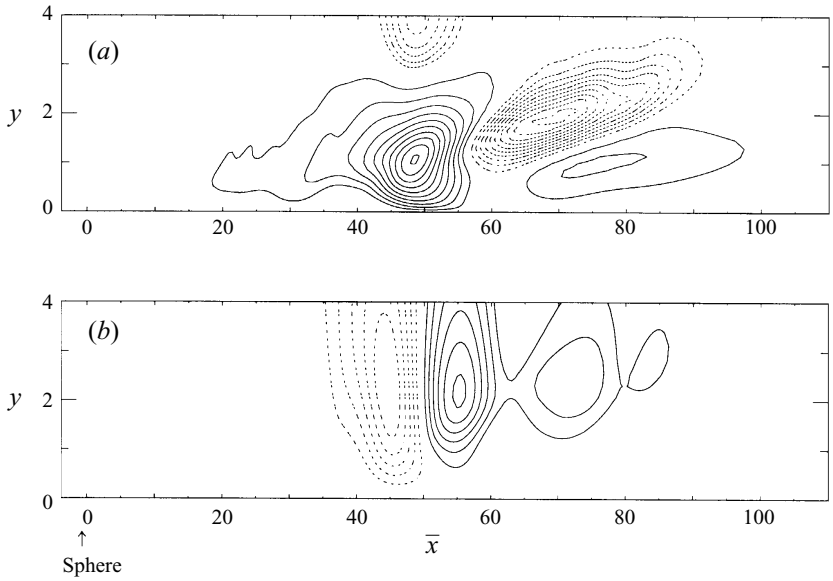


FIGURE 20. As figure 19 but at $z = 2\pi$.

of the computation there is no evidence of the disturbance as both portions convect out of the computational domain. Only closely spaced contours in the near vicinity of the sphere remain, indicating the continuous shedding of the hairpin vortices.

The results obtained in this computation demonstrate that due to the interaction of the sphere with the boundary layer, an isolated disturbance is induced which behaves in a manner similar to the disturbances investigated in § 3 and by Breuer & Haritonidis (1990), Breuer & Landahl (1990), and Henningson *et al.* (1993). The transient portion leaves the computational domain with the wave portion of the disturbance trailing behind inducing a decaying low-frequency T-S wave in the flow field. There is no sudden transition to turbulence, rather the disturbance propagates away leaving behind the Tollmien-Schlichting wave which, despite the presence of inflectional velocity profiles due to the high-shear layer in the wake of the sphere, does not become unstable.

4.2. *Supercritical case*

For this computation, the location and the dimensions of the sphere were as in the subcritical case, but the Reynolds number was increased to a supercritical value. This was achieved by increasing the Reynolds number at the inflow resulting in a sphere Reynolds number of $Re_d = 494$ and a boundary-layer Reynolds number at the sphere location of $Re_{\delta_p^*} = 795$. The height of the top of the sphere from the wall with respect to δ_p was $k^*/\delta_p = 0.4058$. The mesh resolution in the computational domain was $306 \times 71 \times 65$ on a domain size of $137.36 \times 75 \times 4\pi$ (table 1). Although the number of points in the spanwise direction was larger than that applied in the subcritical case, the spanwise length of the domain was also increased, and the spanwise resolution did not change between the two cases. The length and resolution of the buffer domain also remained the same.

This case resulted in the development of complex fluid motion akin to turbulence. The available machine resolution enabled the simulation of an incipient turbulent state characterized by the formation of a turbulent wedge, but was insufficient for

https://doi.org/10.1017/S0022112097006198 Published online by Cambridge University Press

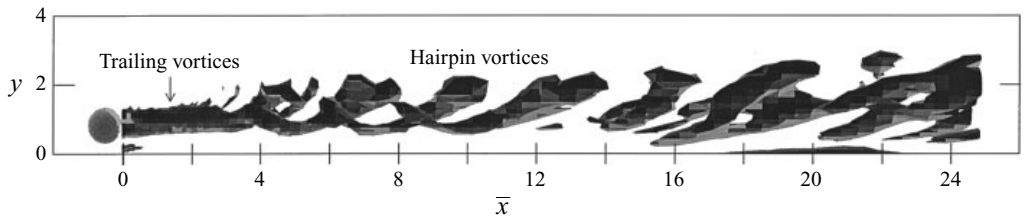


FIGURE 21. Supercritical case: side view of isosurfaces of streamwise vorticity. The level is −0.15.

the simulation of a statistically steady fully developed turbulent flow. Consequently, this high-Reynolds-number simulation captured only the salient characteristics of transitional behaviour and early turbulence in this complex flow field.

The wake downstream of the sphere in this case can be categorized into several regions where particular events occur: (i) the near-flow region of the sphere $0 \leqslant \overline{x} \leqslant 2.35$, (ii) the appearance of a pair of fixed trailing vortices over ($0 \leqslant \overline{x} \leqslant 3.026$), (iii) a short region spanning approximately ($3.026 \leqslant \overline{x} \leqslant 15$) where distinctive hairpin vortices are shed and then convected downstream as they break down to become part of (iv) a wedge of complex flow. The development of the flow field from the initial stages to the full wedge involves the formation of a three-dimensional disturbance which breaks down into a structure similar to a turbulent spot.

4.2.1. *Trailing and hairpin vortices*

Figure 21 presents instantaneous constant-streamwise-vorticity surfaces over $0 \leqslant \overline{x} \leqslant 28$ at $t = 215.4$. The streamwise extent of the trailing vortices downstream of the sphere is much shorter and the shedding of the hairpin vortices begins at streamwise locations closer to the sphere in this case. At this particular snapshot in time, four distinct vortices appear immediately downstream of the trailing vortices which resemble the vortices shed in the subcritical case (figure 5). These hairpin vortices are stretched as they are convected downstream and their heads are lifted up into the free stream to a maximum height of $y \approx 2.6$. In comparison with the subcritical case, the hairpin heads in the supercritical case reach greater distances above the plate at streamwise locations closer to the sphere, e.g. at $\overline{x} = 10.6$ the heights of the hairpins are $y \approx 2$ and $y \approx 2.6$ in the sub- and supercritical cases, respectively. However, the angle of inclination of the legs with respect to the wall is around 25°, similar to the angle observed in the supercritical case. Downstream of these four vortices, the previously shed hairpin vortices become more irregular as the legs move toward the wall and their heads move upward higher into the free stream. This behaviour of the hairpin vortices is in accordance with observations obtained by Vincent & Petrie (1993).

4.2.2. *Time evolution and Fourier analysis*

The time signals extracted from this computation are not as clear as in the subcritical case where the dominant frequencies present in the flow field correspond to the frequency of the shedding of hairpin vortices and the decaying influence of the wave part of the isolated disturbance. In the supercritical case, the complexity of the wake is revealed by the irregularity of the time signals even in the region where the hairpin vortices are shed. This behaviour is evident in time traces recorded at $\overline{x} = 10.6$, $z = 2\pi$, and $y = 1.86$ (at the top height of the hairpin vortices at this streamwise location) presented in figure 22(*a*). The time signal is relatively uniform revealing a

https://doi.org/10.1017/S0022112097006198 Published online by Cambridge University Press

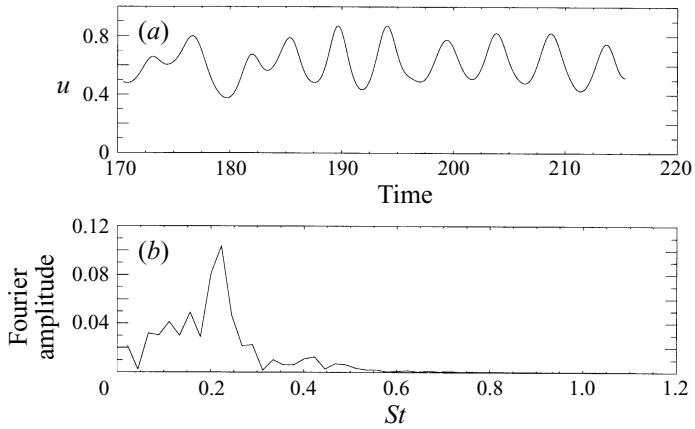


FIGURE 22. Supercritical case: (*a*) time evolution of streamwise velocity over ten vortex shedding periods and (*b*) Fourier spectrum of streamwise velocity vs. Strouhal number at $\overline{x} = 10.6$, $y = 1.86$, and $z = 2\pi$.

spike in the Fourier spectrum at $St = 0.22$ associated with the hairpin vortex shedding. The Strouhal frequency ($St = 0.22$) obtained in this case is in good agreement with the experimental results of Vincent & Petrie (1993) ($St \approx 0.23$ at $Re_d = 494$). The time signals in the hairpin shedding region also exhibit phase shifts between various normal and spanwise measurement positions (not shown) in accordance with the hairpin vortex structure (§ 4.1.1). There is no evidence of a low-frequency component in these time traces (or in others at different locations) associated with a T-S wave, because the wave portion of the disturbance is weaker than the transient part which induces the rapid breakdown of the isolated disturbance into a turbulent-like spot (§ 4.2.3).

4.2.3. *Three-dimensional isolated disturbance*

In a manner similar to the low-Reynolds-number case, a three-dimensional isolated disturbance induced by the interaction of the sphere with the boundary layer develops. A flow field arises in the early stages of the computation which closely matches the initial stages of the subcritical case (figure 18). Instantaneous streamwise velocity contours reveal the time evolution of the planform of this structure in $(\overline{x}, z)$-planes at $y = 1.3$ (figure 23). The spanwise direction has been magnified in these figures in order to obtain a more detailed view of the structure; under normal conditions, it is much thinner and the streamwise stretching of the structure is more pronounced. The breakdown appears to originate at the upstream part of the disturbance in a manner similar to the breakdown of an isolated disturbance investigated by Henningson *et al.* (1993), and as the disturbance moves downstream, the complexity of the flow field influences the downstream portion of the disturbance. The increase in the streamwise length of the spot is evident as the downstream portion propagates faster than the upstream portion at speeds estimated as ≈ 0.74 and ≈ 0.38, respectively. These velocities are deduced by extracting the streamwise locations of the leading and trailing edges of the structure in the (x, z)-planes shown in figure 23 for each of the instantaneous solutions. Note that the speed of the downstream part closely corresponds to the local mean velocities in accordance with the development of the transient part of an isolated three-dimensional disturbance, whereas the upstream portion is moving at a velocity closer to the most unstable T-S wave (0.37) predicted

https://doi.org/10.1017/S0022112097006198 Published online by Cambridge University Press

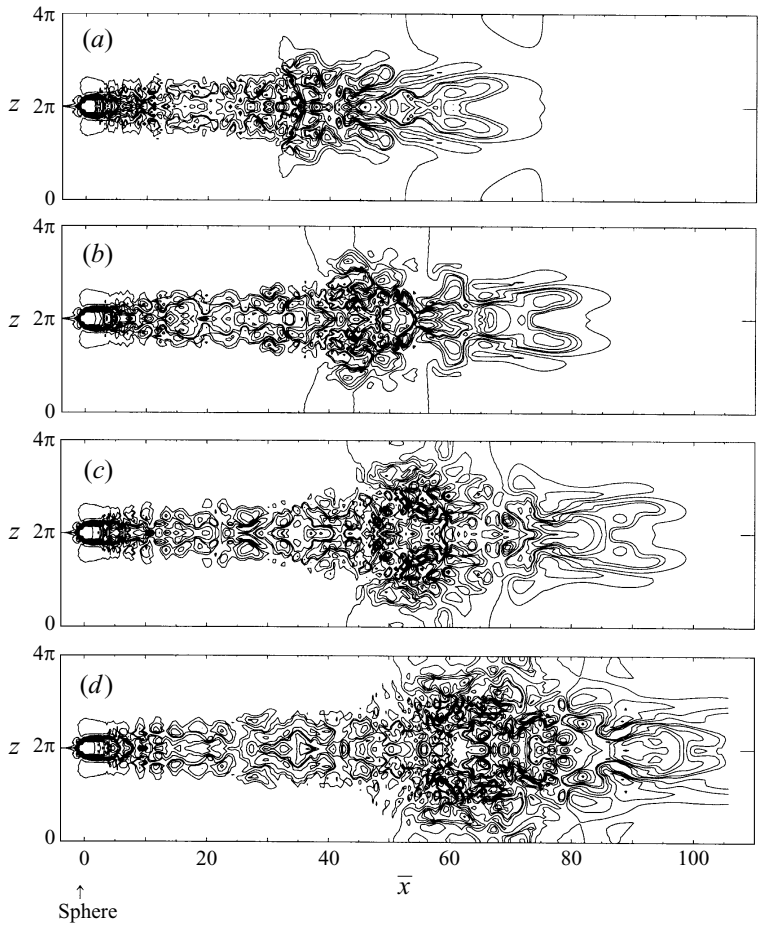


FIGURE 23. Supercritical case: time evolution of streamwise velocity contours in the $(\overline{x}, z)$-plane at $y = 1.3$. (*a*) $t = 98.74$, (*b*) $t = 116.69$, (*c*) $t = 134.64$, and (*d*) $t = 152.6$.

by linear stability analysis for the Reynolds numbers used in this case. The wave part of the disturbance can be briefly observed in the $(\overline{x}, y)$-plane off the centreline at $z = 4\pi$ in v contours in figure 24 at $t = 98.74$ and $t = 116.69$. The position of the wave part corresponds to the upstream portion of the disturbances shown in planview in figures 23(*a*) and 23(*b*).

In comparison with the propagation velocities of fully developed turbulent spots in the boundary layer, the disturbance obtained in the current computation travels at a slower speed. Experimental studies cite leading- and trailing-edge velocities of 0.9 and 0.5, respectively (Riley & Gad-el-Hak 1985), independent of the Reynolds number. Computations simulating boundary-layer turbulent spots (Henningson, Spalart & Kim 1987) also obtained higher propagation rates of the leading and trailing portions of a fully developed turbulent spot as well as a higher spanwise spreading rate of 0.065; the spanwise growth of the structure in the current study is estimated as 0.0275. In the studies of Henningson *et al.* (1987), the spot was generated by a high-amplitude Gaussian impulse of height $\frac{1}{3}\delta$ introduced in the boundary layer. The development of their disturbance in the initial stages also exhibited lower trailing- and leading-edge propagation velocities than observed in the final stages when their

https://doi.org/10.1017/S0022112097006198 Published online by Cambridge University Press

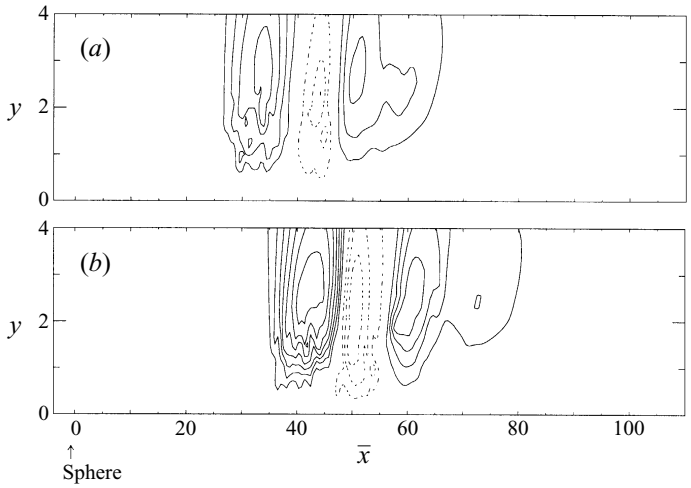


FIGURE 24. Supercritical case: normal velocity contours indicating the wave part of the disturbance in the $(\overline{x}, y)$-plane at $z = 4\pi$. (*a*) $t = 98.74$ and (*b*) $t = 116.69$.

disturbance matured into a fully turbulent spot. In the current study, it is possible that the disturbance will follow a similar route, ultimately evolving into a turbulent spot. The shape of the disturbance is similar to the physical characteristics associated with turbulent spots in the boundary layer, i.e. an arrow-shaped planform with the apex pointing downstream and a 'head' which is stretched ahead of the spot creating an overhang of fluid.

The lower spanwise spreading rate of the disturbance in comparison with the computational studies of Henningson *et al.* (1987) is due to the shorter periodicity length of the computational domain implemented in the current study. These computations model the effect of an infinite array of spheres in the spanwise direction and the interference of the wakes of the spheres attenuates the spreading of the disturbance. This characteristic also influences the half-angle of the disturbance measured from the symmetry line ($\phi = 7.3°$), which is smaller than half-angles ($\phi = 10°$) observed in previous studies (Riley & Gad-el-Hak 1985; Henningson *et al.* 1987).

The experiments of Blackwelder *et al.* (1992) showed the production of a turbulent spot when an isolated sphere entered the boundary layer. The sphere hits the wall and then rolls along it creating a wake as the spot quickly moves ahead downstream. The current results suggest that the turbulent spot observed by Blackwelder *et al.* (1992) evolved from an isolated three-dimensional disturbance generated by the interaction of the sphere and the boundary layer.

4.2.4. *Turbulent wedge*

The passage and breakdown of the isolated disturbance yields to the development of an incipient turbulent wedge in the wake of the sphere. The appearance of the turbulent wedge is in accordance with experimental results at supercritical Reynolds numbers (Mochizuki 1961; Hall 1967; Vincent & Petrie 1993). The instantaneous streamwise velocity contours presented in figure 25 clearly depict the top and side views of the wedge at $t = 215.4$. The wedge forms a half-angle of 4°–5° with the vertex placed at the sphere measured from the centreline. Experiments have shown half-angles of the the fully turbulent wedge ranging from 5°–6.4° (Schubauer & Klebanoff 1955; Mochizuki 1961; Norman 1971).

https://doi.org/10.1017/S0022112097006198 Published online by Cambridge University Press

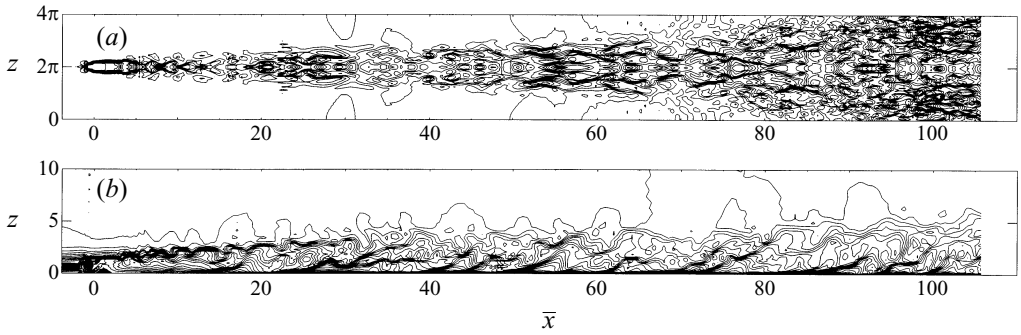


FIGURE 25. Supercritical case: instantaneous streamwise velocity contours at $t = 215.4$: (a) the $(\overline{x}, z)$-plane at $y = 1.3$ and (b) the $(\overline{x}, y)$-plane at $z = 2\pi$.

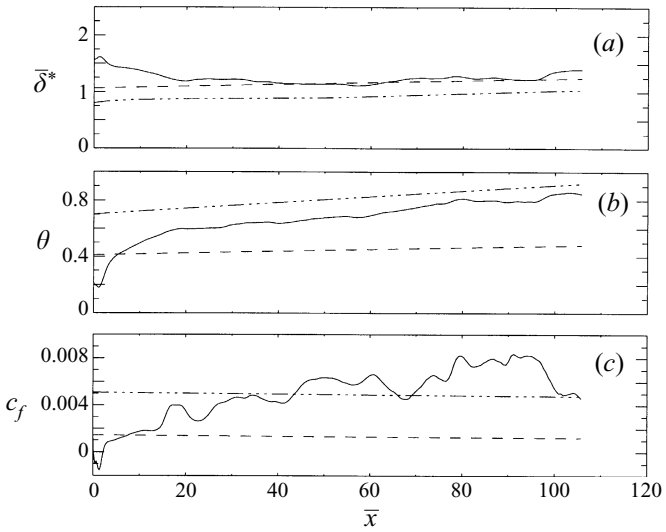


FIGURE 26. Supercritical case: streamwise distribution of (a) non-dimensional boundary layer displacement thickness, $\overline{\delta}^*$, (b) momentum thickness, θ, and (c) skin friction coefficient, c_f, downstream of the sphere. ——— , current solution; — — — , laminar boundary layer solution; and — ··· —, turbulent boundary layer; empirical relations (4.7), (4.9).

4.2.5. *Boundary layer characteristics*

Figure 26 reveals the streamwise distribution downstream of the sphere of boundary-layer displacement thickness, momentum thickness, and skin friction coefficient at $z = 2\pi$. For comparison, the distributions corresponding to the Blasius (laminar) solution and the empirical relations for turbulent boundary layers are included in figure 26. The turbulent boundary layer relations for $10^5 \leqslant Re_{x^*} \leqslant 10^9$ (White 1974) are (in a non-dimensional form consistent with the current computation)

$$\overline{\delta}^* \approx 0.018 \frac{Re_{x^*}^{6/7}}{Re_{\delta_o^*}}, \tag{4.7}$$

$$\theta \approx 0.0142 \frac{Re_{x^*}^{6/7}}{Re_{\delta_o^*}}, \tag{4.8}$$

https://doi.org/10.1017/S0022112097006198 Published online by Cambridge University Press

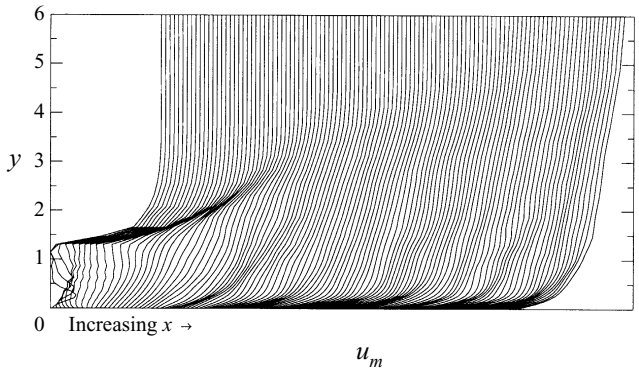


FIGURE 27. Supercritical case: normal profiles of streamwise mean velocity at every other streamwise location downstream of the sphere at $z = 2\pi$. Each profile is offset by $\Delta u = 0.02$.

and

$$c_f \approx \frac{0.455}{\ln^2 0.06 Re_{x^*}}. \tag{4.9}$$

Each of the distributions shows similar characteristics to those exhibited by the subcritical case (figure 9) at streamwise locations near the sphere, i.e. an increase and decrease in boundary layer displacement and momentum thickness, respectively, resulting in a marked increase in shape factor, and a region of negative skin friction coefficient corresponding to the wall separation bubble. Further downstream, the distribution of displacement thickness (figure 26*a*) decreases and follows the laminar case; in contrast, the momentum thickness (figure 26*b*) increases and approaches the turbulent value. The Reynolds number based on the momentum thickness in the turbulent wedge region varies from $Re_\theta = 580$ to 643. Far downstream, the combined effects of $\overline{\delta}^*$ and θ result in a decrease in the shape factor to ≈ 1.6, which is in good agreement with results obtained in previous studies investigating low-Reynolds-number turbulent boundary layers: at $Re_\theta = 600$, Purtell, Klebanoff & Buckley (1981) measured $H \approx 1.58$, and the computational study by Spalart (1988) yielded $H \approx 1.5$ for $Re_\theta = 670$, whereas the empirical formulas for H obtain a constant value of 1.3. The skin friction coefficient increases from the laminar values, overshooting the turbulent profile (figure 26*c*). The fluctuating nature of the quantities presented in figure 26 indicates that the computation has not reached a statistically steady turbulent state.

4.2.6. *Velocity profiles*

The streamwise development of the normal profiles of streamwise mean velocity at $z = 2\pi$ are presented in figures 27 and 28. We emphasize here that the mean velocity in this case is not a true mean, since the flow field has not reached a quasi steady state; rather we are examining the time average of the flow field computed over the last portion of the simulation. The oscillations observed in the normal profiles near the sphere for this case (figure 27) reflect one of the effects of the virtual boundary method when it is applied with spectral methods. The virtual boundary acts as a discontinuity in the spectral representation of the flow field, thus causing spatial oscillations (Gibbs phenomenon). These oscillations remain at a fixed amplitude and previous analysis (Saiki & Biringen 1996) has demonstrated that they do not affect the solution.

https://doi.org/10.1017/S0022112097006198 Published online by Cambridge University Press

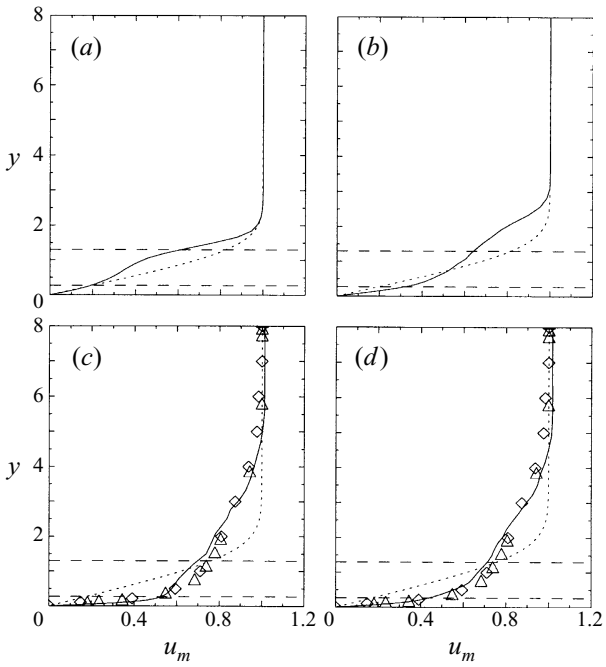


FIGURE 28. Supercritical case: comparison of streamwise mean velocity profiles at the centreline of the turbulent wedge with experimental studies of turbulent boundary layers. (*a*) $\overline{x} = 53.85$, $Re_\theta = 515$, (*b*) $\overline{x} = 75.46$, $Re_\theta = 582.77$, (*c*) $\overline{x} = 91.67$, $Re_\theta = 597.38$, and (*d*) $\overline{x} = 102.5$, $Re_\theta = 643.4$. Experimental results from Purtell *et al.* (1981); △, $Re_\theta = 500$ and ⋄, $Re_\theta = 700$. The Blasius profile is denoted by ·····.

In a manner similar to the subcritical case, the profiles in the near vicinity of the sphere reflect the appearance of the separation bubbles and exhibit an inflection point at normal locations above the top of the sphere corresponding to the top shear layer. The inflectional nature of the profiles is not as pronounced in this case as it is in the lower-Reynolds-number case (figures 10 and 12); however, the top shear layer is still clearly present (figure 27). In association with the motion of the hairpin vortices, the shear layer is lifted upward higher than in the subcritical case. Further downstream, the inflection points of the profiles also move upward and the distributions begin to flatten near the wall, deviating considerably from the laminar profiles. Comparison of the mean velocity with experimental studies of low-Reynolds-number turbulent boundary layers (Purtell *et al.* 1981) provides evidence that the flow field is approaching a turbulent state (figure 28).

The root-mean-square profiles for this case are presented in figure 29 where the y-coordinate has been rescaled by the local boundary layer thickness, δ^*, in order to compare the current results with those of previous studies. The profiles reveal sharp maxima at the top of the sphere and in the hairpin vortex shedding region in a manner similar to the subcritical case (figure 11). The maxima above the sphere decrease in relative amplitude and move away from the wall as the heads of the hairpin vortices rise upwards and the profiles become fuller. The r.m.s. distributions further downstream (figure 29) continue to thicken in the normal direction and by the last streamwise position shown, a second peak of amplitude 0.175 becomes dominant (figure 29*d*). The maximum amplitude is comparable with maximum r.m.s. values obtained by Acarlar & Smith (1987), Klebanoff *et al.* (1992), and Vincent & Petrie

https://doi.org/10.1017/S0022112097006198 Published online by Cambridge University Press

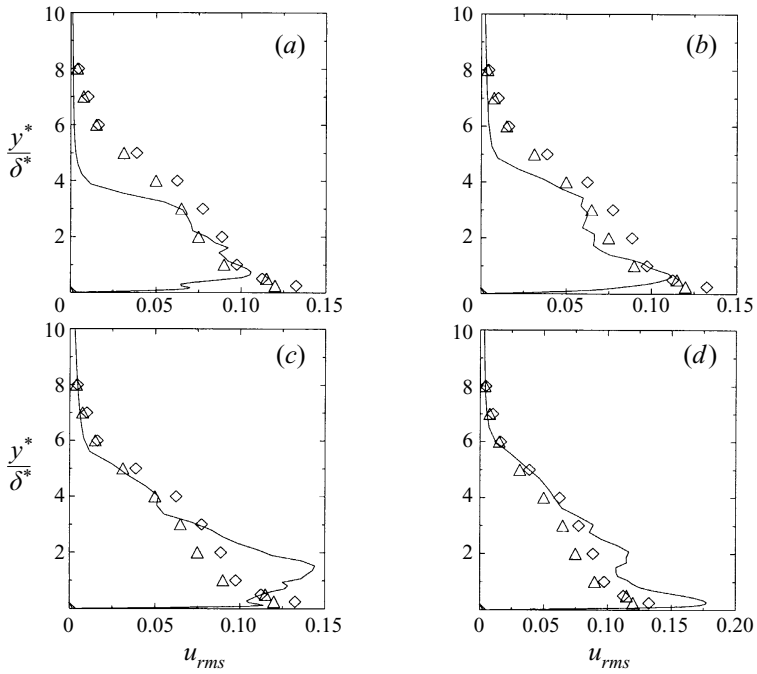


FIGURE 29. Supercritical case: comparison of streamwise root-mean-square velocity profiles at the centreline of the turbulent wedge with experimental studies. The streamwise positions are the same as in figure 28. Experimental results from Purtell *et al.* (1981): △, $Re_\theta = 700$; and Klebanoff *et al.* (1992); ◇, $Re_\theta = 745$. Note that the y-coordinate is non-dimensionalized by the local boundary layer thickness, δ^*.

(1993). These profiles reveal a trend towards turbulence even though the distributions reveal that a statistically steady turbulent state has not yet been reached. Figure 29 also compares four r.m.s. profiles from the current computation with the r.m.s. profiles obtained by Purtell *et al.* (1981) in turbulent boundary layers and by Klebanoff *et al.* (1992) in the turbulent wedge of a wake of a hemisphere in the boundary layer, revealing their close similarity. These comparisons indicate that the computational results are representative of low-Reynolds-number turbulent flows.

The spanwise distributions of mean streamwise velocities are presented in figure 30. The mean profiles reflect the same behaviour observed in the subcritical case related to the rotational motion of the hairpin vortices with a velocity deficit at the centreline, $z = 2\pi$, and two maxima surrounding the spanwise extent of the sphere (figure 30*a, b*). Further downstream, the momentum deficit can be observed at higher normal locations above the wall as the wake breaks down forming the turbulent wedge (figure 30*d*).

5. Summary and conclusions

The focus of the current study was to numerically investigate the effects of a spherical particle on boundary layer transition. It has long been recognized that particles cause transition to turbulence in boundary layers, and several flow visualization studies have established the characteristics of the sphere wake, defining sub- and supercritical regimes. To further substantiate these previous studies we pursued this problem with several goals: (i) to capture the sub- and supercritical behaviour

https://doi.org/10.1017/S0022112097006198 Published online by Cambridge University Press

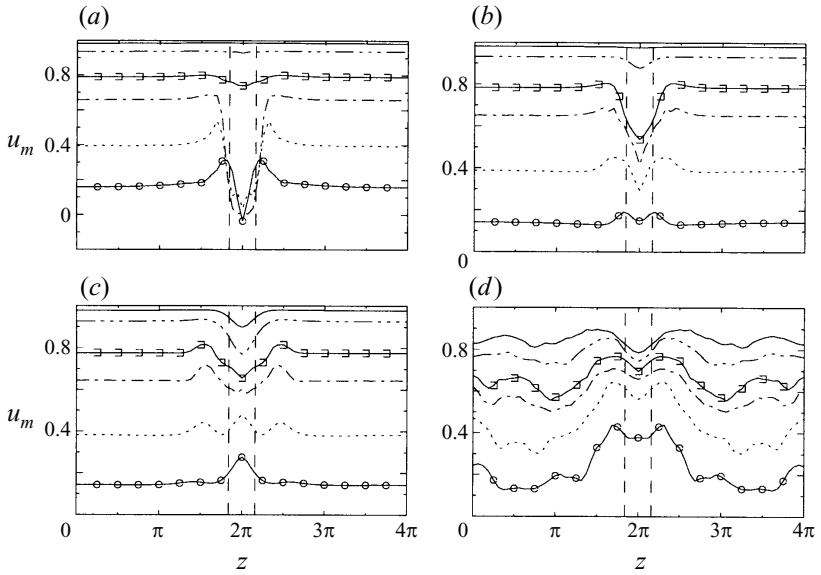


FIGURE 30. Supercritical case: spanwise profiles of streamwise mean velocity at the same streamwise and normal positions listed in figure 13.

of the sphere wake observed in experimental studies and (ii) to determine if three-dimensional isolated disturbances associated with the linear lift-up mechanism are characteristic of particle-induced transition in the boundary layer.

Simulations of an isolated three-dimensional disturbance represented by two counter-rotating pairs of streamwise vortices of high amplitude were performed repeating the temporal work of Breuer & Landahl (1990) using a spatial computational model. These calculations were completed in order to provide data for comparison with the sphere cases and to assess the normal mesh resolution requirements in properly capturing the development of the disturbance, confirming the observations of Henningson *et al.* (1993). As demonstrated by Breuer & Haritonidis (1990) and Breuer & Landahl (1990), such disturbances are characterized by two parts: a transient part and a wave part. The lift-up mechanism is associated with the transient part and is activated by the three-dimensionality of the flow field and the presence of mean shear while the wave part is associated with Tollmien–Schlichting wave behaviour (Breuer & Haritonidis 1990). The growth and dominance of the transient part of the disturbance can lead to transition to turbulence bypassing the T-S linear instability route.

The results from two sphere cases were examined: a subcritical case where hairpin vortices are shed into the sphere wake and a supercritical case where a wedge of incipient turbulence develops. The characteristics of the sphere wake were evaluated and comparison with previous experimental results reveals good agreement. In both the sub- and supercritical cases, the interaction of the sphere with the boundary layer induces an isolated three-dimensional disturbance which develops in a two-part manner similar to the evolution of disturbances outlined above; however, the behaviour of the disturbance differs between the two cases.

In the subcritical case, the transient part decays as it is convected downstream, while the wave part introduces a T-S wave into the flow field. The presence of the T-S wave does not lead to transition to turbulence, rather the wave amplitude exhibits a gradual decay after the wave part of the disturbance leaves the domain, while the

https://doi.org/10.1017/S0022112097006198 Published online by Cambridge University Press

hairpin vortices shed into the wake simply decay as they convect downstream. With an increase in Reynolds number, the disturbance is dominated by the transient part, and as it travels downstream it forms a structure similar to a turbulent spot. The wave part developing at the rear portion of the spot is much weaker and the spot breaks down to form a wedge of incipient turbulence in the wake. The shed hairpin vortices also break down, feeding into the 'turbulence' in the wedge.

In summary, the above observations link three-dimensional disturbances to the effects of spheres in the boundary layer. The Reynolds number affects the transient part, dictating whether or not transition to turbulence occurs. In the low Reynolds number case, viscosity dampens the amplitude of the transient part, while for the high Reynolds number case the transient part grows to sufficiently high amplitude to cause the disturbance to break down.

The current results correlate well with the experimental observations of Blackwelder *et al.* (1992) and R. Blackwelder & P. Tanaguichi (personal communication) which revealed that as a sphere enters the boundary layer, the sphere wake produces streamwise vortices which convect downstream forming a turbulent spot. The present study offers an explanation for the mechanism behind the breakdown of the streamwise vortices.

This work was supported by ONR under grant number DOD N00014-94-1-0923. The authors wish to thank program director James A. Fein for his continued interest in this work. The authors also acknowledge the helpful comments of the anonymous referees.

REFERENCES

Acarlar, M. S. & Smith, C. R. 1987 A study of hairpin vortices in a laminar boundary layer. Part 1. Hairpin vortices generated by a hemisphere protuberance. *J. Fluid Mech.* **175**, 1.

Blackwelder, R. F., Browand, F. K., Fisher, C. & Tanaguichi, P. 1992 Initiation of turbulent spots in a laminar boundary layer by rigid particulates. *Bull. Am. Phys. Soc.* **37**, 1812.

Breuer, K. S. & Haritonidis, J. H. 1990 The evolution of a localized disturbance in a laminar boundary layer. Part 1. Weak disturbances. *J. Fluid Mech.* **220**, 569.

Breuer, K. S. & Landahl, M. T. 1990 The evolution of a localized disturbance in a laminar boundary layer. Part 2. Strong disturbances. *J. Fluid Mech.* **220**, 595.

Danabasoglu, G. 1992 Spatial simulation of transition in wall-bounded shear flows: Active control and effects of surface roughness. PhD thesis, Department of Aerospace Engineering Sciences, University of Colorado, Boulder, Colorado.

Danabasoglu, G., Biringen, S. & Streett, C. L. 1991 Spatial simulation of instability control by periodic suction blowing. *Phys. Fluids* A **3**, 2138.

Goldstein, D., Handler, R. & Sirovich, L. 1993 Modeling a no-slip flow boundary with an external force field. *J. Comput. Phys.* **105**, 354.

Goldstein, D., Handler, R. & Sirovich, L. 1995 Direct numerical simulatio of turbulent flow over a modelled riblet covered surface. *J. Fluid Mech.* **302**, 333.

Hall, G. R. 1967 Interaction of the wake from bluff bodies with an initially laminar boundary layer. *AIAA J.* **5**, 1386.

Henningson, D. S., Lundbladh, A. & Johansson, A. V. 1993 A mechanism for bypass transition from localized disturbances in wall-bounded shear flows. *J. Fluid Mech.* **250**, 169.

Henningson, D. S., Spalart, P. R. & Kim, J. 1987 Numerical simulations of turbulent spots in plane Poiseuille and boundary-layer flow. *Phys. Fluids* **30**, 291.

Jordinson, R. 1970 The flat plate boundary layer. Part 1. Numerical integration of the Orr-Sommerfeld equation. *J. Fluid Mech.* **43**, 801.

Joslin, R. D., Streett, C. L. & Chang, C.-L. 1993 Spatial direct numerical simulation of boundary-layer transition mechanisms: Validation of PSE theory. *Theor. Comput. Fluid Dyn.* **4**, 271.

https://doi.org/10.1017/S0022112097006198 Published online by Cambridge University Press

Klebanoff, P. S., Cleveland, W. G. & Tidstrom, K. D. 1962 The three-dimensional nature of boundary-layer instability. *J. Fluid Mech.* **12**, 1.

Klebanoff, P. S., Cleveland, W. G. & Tidstrom, K. D. 1992 On the evolution of a turbulent boundary layer induced by a three-dimensional roughness element. *J. Fluid Mech.* **237**, 101.

Landahl, M. T. 1975 Wave breakdown and turbulence. *SIAM J. Appl. Maths* **28**, 735.

Landahl, M. T. 1980 A note on an algebraic instability of inviscid parallel shear flows. *J. Fluid Mech.* **98**, 243.

Mochizuki, M. 1961 Smoke observation on boundary layer transition caused by a spherical roughness element. *J. Phys. Soc. Japan* **16**, 995.

Morkovin, M. V. 1985 Guide to experiments on instability and laminar-turbulent transition in shear layers. Notes for AIAA short course.

Norman, R. S. 1971 On obstacle generated secondary flows in laminar boundary layers and transition to turbulence. PhD thesis, Illinois Institute of Technology, Chicago, Illinois.

Purtell, L. P., Klebanoff, P. S. & Buckley, F. T. 1981 Turbulent boundary layer at low Reynolds number. *Phys. Fluids* **24**, 802.

Riley, J. J. & Gad-el-Hak, M. 1985 The dynamics of turbulent spots. In *Frontiers in Fluid Mechanics* (ed. S. M. Davis & J. L. Lumley), pp. 123–155. Springer.

Saiki, E. M. 1995 Spatial numerical simulation of boundary layer transition: Effects of a spherical particle. PhD thesis, Department of Aerospace Engineering Sciences, University of Colorado, Boulder, Colorado.

Saiki, E. M. & Biringen, S. 1996 Numerical simulation of a cylinder in uniform flow: Application of a virtual boundary method. *J. Comput. Phys.* **123**, 450.

Saiki, E. M., Biringen, S., Danabasoglu, G. & Streett, C. L. 1993 Spatial simulation of secondary instability in plane channel flow: Comparison between H- and K-type disturbances. *J. Fluid Mech.* **253**, 485.

Schubauer, G. B. & Klebanoff, P. S. 1955 Contributions on the mechanics of boundary-layer transition. *NACA Tech. Note* 3489.

Sirovich, L. 1967 Initial and boundary value problems in dissipative gas dynamics. *Phys. Fluids* **10**, 24.

Sirovich, L. 1968 Steady gasdynamic flows. *Phys. Fluids* **11**, 1324.

Spalart, P. R. 1988 Direct simulation of a turbulent boundary layer up to $Re_\theta = 1410$. *J. Fluid Mech.* **187**, 61.

Streett, C. L. & Macaraeg, M. G. 1989 Spectral multi-domain for large-scale fluid dynamic simulations. *Appl. Numer. Maths* **6**, 123.

Vincent, D. C. & Petrie, H. L. 1993 Transition induced by a spherical particle in a laminar boundary layer. *AIAA Paper* 93-2902.

White, F. M. 1974 *Viscous Fluid Flow*. McGraw-Hill.

https://doi.org/10.1017/S0022112097006198 Published online by Cambridge University Press